Michael Stadlhofer, BSc

Femtosecond Photodynamics of Magnesium Molecules and Clusters inside Helium Nanodroplets

MASTER'S THESIS

to achieve the university degree of

Diplom-Ingenieur

Master's degree programme: Technical Physics

submitted to

Graz University of Technology

Supervisor

Assoc. -Prof. Dipl. -Ing. Dr. Markus Koch

Institute of Experimental Physics

Graz, October 2020

AFFIDAVIT

I declare that I have authored this thesis independently, that I have not used other than the declared sources/resources, and that I have explicitly indicated all material which has been quoted either literally or by content from the sources used. The text document uploaded to TUGRAZonline is identical to the present master's thesis.

Date, Signature

Abstract

The formation of bonds between atoms is a dynamical process that is difficult to observe in real time. Superfluid helium nanodroplets doped with Mg atoms present a new opportunity to study bond formation using time resolved photoelectron spectroscopy. Inside the superfluid a metastable magnesium structure can form, in which individual Mg atoms are separated at approximately 10 Å distance due to a small He barrier in between the Mg atoms. Photoexcitation of this so called magnesium foam starts a collapse, which releases energy and populates highly excited electronic states while bonds between the atoms are formed. So far, this ultrafast energy release mechanism has been observed with strong-field time-resolved and non-time-resolved spectroscopic techniques, but not with time-resolved spectroscopic techniques, which would provide insight into the transient changes of the electronic states of the system.

In this work the photoinduced dynamics of magnesium doped helium droplets were investigated using femtosecond pump-probe photoelectron and ion spectroscopy. For high Mg doping conditions a transient signal, which likely originates from the magnesium foam collapse and subsequent bond formation, has been identified. An estimation for the collapse time of (300 ± 40) fs can be given. Photoelectron transients corresponding to dynamics of an initially compact magnesium cluster have also been observed. Additionally, a delayed ion mass signal increase was measured which might be explained by either a foam collapse or by delayed ejection from the helium droplet due to the attractive interaction between helium and ionic species. Further measurements using photoelectron-photoion-coincidence spectroscopy could allow to differentiate between those two processes. The dependence of the photoelectron signals on the pump wavelength, the pump and probe pulse power, as well as the magnesium doping level were studied. These characterizations allowed an assignment of the observed photoelectron bands and dynamics to single Mg atoms, compact Mg clusters and metastable Mg foam.

The obtained results represent the first direct observation of photoinduced bond formation inside a quantum fluid. Further tests using photoelectron-photoion-conincidence spectroscopy will provide more insight in the nuclear dynamics of this process. In addition to the Mg foam measurements a photoelectron energy shift caused by the bubble expansion around single excited Mg atoms inside the droplets was found. Dynamics which can be attributed to Mg dimers were also observed.

Kurzfassung

Die Bildung von Bindungen zwischen Atomen ist ein dynamischer Prozess, der in Echtzeit sehr schwierig zu beobachten ist. Mit Mg Atomen dotierte, superfluide Helium-Nanotröpfchen bieten eine neue Möglichkeit, die Bildung von Bindungen mithilfe von zeitaufgelöster Photoelektronenspektroskopie zu untersuchen. Im Superfluid kann sich eine metastabile Magnesiumstruktur ausbilden, in der die einzelnen Mg Atome von einer 10 Å großen He Barriere getrennt sind. Photoanregung bringt diese Struktur, die Mg-Schaum genannt wird, zum Kollabieren und ermöglich die Bindung der Mg Atome. Hierbei wird Energie frei, die Elektronen in hochangeregte Zustände bringt. Bisher wurde dieser ultraschnelle Energiefreisetzungsmechanismus mit zeitaufgelösten Starkfeld und nicht zeitaufgelösten spektroskopischen Methoden untersucht, aber nicht mit zeitaufgelösten spektroskopischen Methoden, die Einblicke in die dynamische Änderungen der elektronischen Zustände des Systems geben würden. In dieser Arbeit wurden die photoinduzierten Dynamiken von mit Magnesium dotierten Heliumtröpfchen mit Hilfe von Femtosekunden-Pump-Probe Photoelektronen- und Ionenspektroskopie untersucht. Für hohe Mg Dotierungsbedingungen der Heliumtröpfchen wurde ein transientes Signal identifiziert, das wahrscheinlich vom Zusammenbruch des Mg-Schaums und der anschließenden Bildung von Bindungen stammt. Die Kollapszeit konnte auf (300 $\pm$ 40) fs abgeschätzt werden. Es wurden auch Photoelektronentransienten beobachtet, die der Dynamik eines anfänglich kompakten Magnesiumclusters entsprechen. Ein verzögerter Anstieg der Ionenmassensignale wurde gemessen, der entweder vom Zusammenbruch des Mg-Schaums oder vom verzögerten Auswurf der Ionen aus dem Tropfen auf Grund der attraktiven Wechselwirkung zwischen Helium und Ion erklärt werden könnte. Weitere Messungen unter Verwendung der Photoelektronen-Photoionen-Koinzidenz Spektroskopie könnten es erlauben zwischen diesen beiden Prozessen zu unterscheiden. Die Abhängigkeit der gemessenen Photoelektronensignale von der Pump Wellenlänge, der Pump und Probe Puls Leistung, sowie von der Menge an Mg in den Heliumtröpchen wurde untersucht. Diese Charakterisierung ermöglichte die Zuordnung der beobachteten Photoelektronen Banden und Dynamiken zu einzelnen Mg Atomen, kompakten Mg Clustern und metastabilem Mg-Schaum.
Die erzielten Resultate stellen die erste direkte Beobachtung von photoinduzierter Bindungsformation in einer Quantenflüssigkeit dar. Weitere Tests mit Photoelektronen-Photoionen-Koinzidenz Spektroskopie werden Einblicke in die Kerndynamiken dieses Prozesses ermöglichen. Zusätzlich zu den Mg-Schaum Messungen wurde eine Photoelektronenenergieverschiebung,

verursacht durch die Blasenexpansion um einzelne angeregte Mg Atome innerhalb der Heliumtröpfchen, gefunden. Dynamiken, die Mg Dimeren zugeordnet werden können, wurden ebenfalls beobachtet.

Contents

Chapter 1

Introduction

Magnesium in helium nanodroplets (^4He_N) was previously studied using frequency domain spectroscopy and strong field pump probe experiments [20] [4] [9]. Experimental evidence from those works hints at the formation and collapse of a metastable magnesium foam inside the helium nanodroplets. Density Functional Theory (DFT) calculations [8] also suggest that Mg forms a metastable foam inside the helium suprafluid. In the course of this thesis, Mg_n in helium nanodroplets were studied using time-resolved Photoelectron (PE) and ion spectroscopy, with the goal to observe the foam collapse dynamics directly in the time domain. A brief introduction to time resolved spectroscopy is given below, followed by a summary of molecular dynamics inside helium droplets. An overview of the scientific literature concerning the Mg foam and foam collapse is presented.

1.1 Time Resolved Spectroscopy

Time resolved spectroscopy uses two light pulses to uncover information about the electronic and nuclear structure of a system. [29] The first pulse (pump) prepares the sample by photoexcitation from the ground state to higher excited states. After some time delay, the second pulse (probe) arrives and ionizes the system. The end products of the ionization, photoelectrons and ions, are detected. The number of detected photoelectrons and ions is proportional to the probability that the ionic state is occupied. The time evolution of the system, after preparation by the pump pulse, can be investigated by varying the pump-probe delay. Dynamics that are usually found are the evolution of nuclear wavepackets on the excited state Potential Energy Surface (PES), or the evolution of electronic wavepackets. The pump-probe measurement is shown schematically for a diatomic molecule in Figure 1.1.

Mathematically, time resolved spectroscopy is described by adding the energy of the electrons in an external electric field ($-\Sigma_i \vec{E}.\vec{r_i}$) to the unperturbed Hamiltonian of the system. The time dependent Schrödinger equation can then be solved numerically, for example by using the rotating wave approximation or time dependent perturbation theory. The results of the numeric calculations can be compared to or aid in the interpretation of the experimental

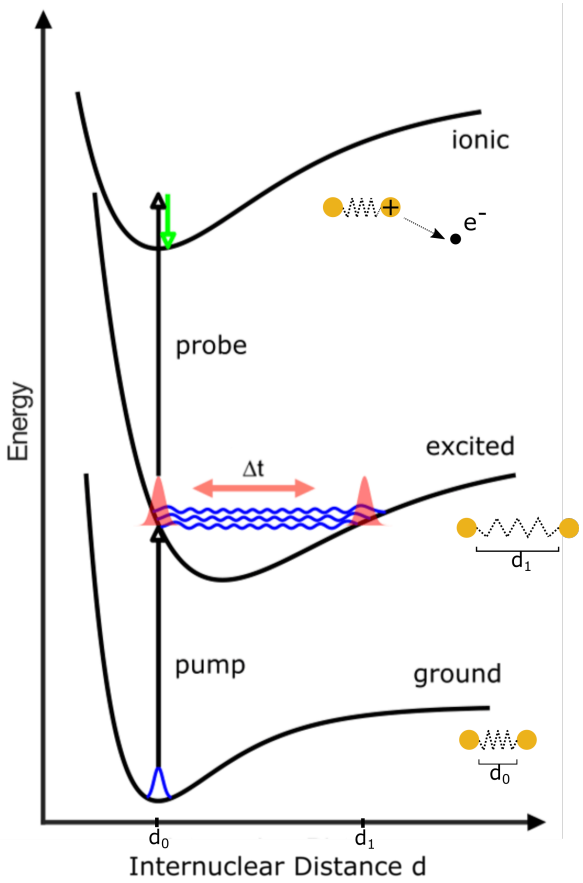

Figure 1.1: The pump-probe measurement process for a diatomic molecule. The pump pulse transports groundstate population of nuclear eigenstates (blue gaussian curve on ground state) to the excited state. On the excited state potential energy surface (or curve in this case) the wavepacket (red) evolves for a time Δt before the probe pulse ionizes the system. This corresponds to an oscillation of the interatomic distance which is similar to a classical vibration of two balls connected by a spring. The green arrow near the top of the image represents the kinetic energy of the photoelectron that is released. Image adapted from [16].

data.

1.1.1 Time Dependent Perturbation Theory for a Diatomic Molecule

The mathematical description of the pump-probe process is explored using the diatomic molecule as an example. [29] The molecule under investigation has three states, namely a (ground state), b (excited state) and c (ionic state) with their corresponding electronic potential energy surfaces. States a and b are resonantly coupled by the pump field $E_1(t)$ (which means the photon energy is the same as the energy difference of states a and b) and states b and c are coupled by the probe field $E_2(t)$. At $t = 0$ the molecule is entirely in the ground state a. First order perturbation theory leads to an expression for the nuclear wavefunction after the pump pulse has perturbed the molecule:

$$\chi_b^{(1)}(R,t) = -i \int_0^t \mathrm{d}t_1 \, e^{-iH_b(t-t_1)} \left(-\mu_{ba} E_1(t_1)\right) e^{-iH_a t_1} \chi_a(R,0) \tag{1.1}$$

This equation can be read right to left to gain intuition on what happens when the pump pulse acts on the system: The nuclear eigenstate χ_a evolves for time t_1 on potential energy surface a. At t_1 the electric field couples the electronic states a and b and tranfers some of the nuclear wavefunction probability of PES a to PES b. The new eigenstate on PES b now evolves for time $t - t_1$.
The expression for the final nuclear wavefunction on PES c is given by second order perturbation theory (in total) or by first order perturbation theory when $\chi_b^{(1)}$ is taken to be the starting wavefunction.

$$\chi_c^{(2)}(R,t) = -i \int_0^t \mathrm{d}t_2 \, e^{-iH_c(t-t_2)} \left(-\mu_{cb} E_2(t_2)\right) \chi_b^{(1)}(R,t_2) \tag{1.2}$$

Note that the vibrational states mentioned here are vibrational eigenstates. In a real experiment the nuclear wavefunction will be a superposition of nuclear eigenstates on a PES. The superposition of nuclear eigenstates can form a wavepacket as seen in Figure 1.1. This introduces a time dependence in the dipole transition element μ_{ab}, since μ_{ab} is calculated from the overlap of electronic and nuclear wavefunctions of the two electronic levels a and b. For a wavepacket that oscillates on an intermediate PES the time dependence of the transition dipole moment can be observed in the measured photoelectron spectra as an oscillation in the electron yield over time. [16] In the case that the intermediate PES is dissociative, the photoelectron spectra will show a peak that shifts in energy over time as the molecule dissociates.

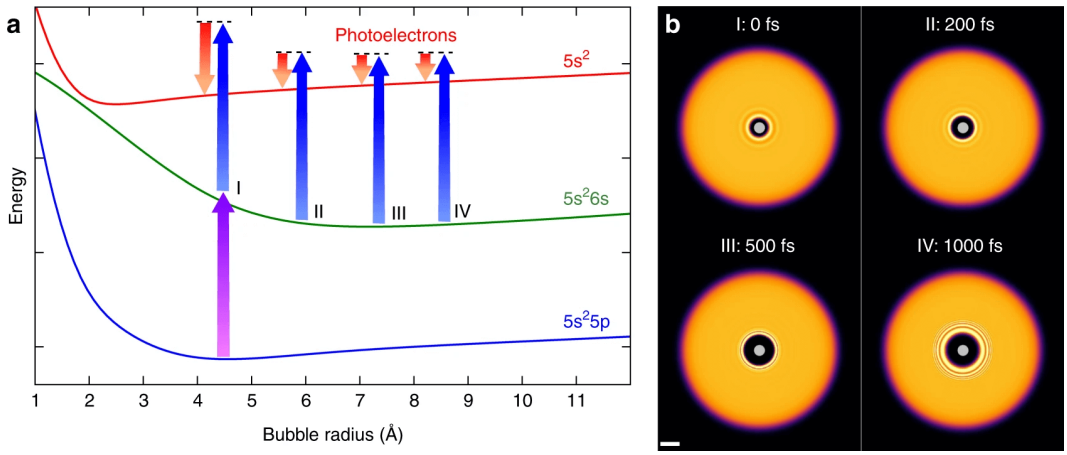

Figure 1.2: (a) The pump-probe detection scheme of the bubble expansion process of the In-He system is shown on the corresponding potential energy curves. (b) Visualization of the helium density over time (calculated from HeDFT) around the In atom. [27]

1.2 Dopant Dynamics Inside Helium Nanodroplets

In this thesis, the system under investigation are magnesium doped helium droplets. The helium environment introduces another layer of complexity to the situation, since the helium density reacts to changes in the electronic state of the dopant. The interplay between dopant and helium dynamics has already been studied for indium atoms. [27] [26]

1.2.1 Dynamics of Indium

The indium atom resides inside a He-free bubble inside the droplet before excitation. This cavity forms due to the pauli-repulsion between the In and He electrons. After excitation with a laser pulse this bubble expands, as a result of the larger electron orbitals of the excited In atom. The dopant is then ejected from the droplet because the excited atom is strongly repelled by the helium. After about 50 ps most of the In has left the droplet [26]. The bubble expansion causes a shift in the ionization potential of indium over time, which can be detected using time resolved photoelectron spectroscopy. Figure 1.2 shows the In-He bubble expansion in terms of the evolution on the bubble radius potential energy curve, as well as the helium density around the In atom over time (obtained from DFT calculations). If the excited indium atom is ionized, it cannot leave the droplet, because atoms in ionic states are strongly attracted by the helium environment. This makes it possible to identify the excited dopant ejection time, since ionized In atoms can only be detected when the ionization happened outside the helium droplet.
For the indium dimer, a wave packet oscillation like the one shown in Figure 1.1, was measured [17]. The ejection time of the dimer was determined to be about 200 ps, which is longer than

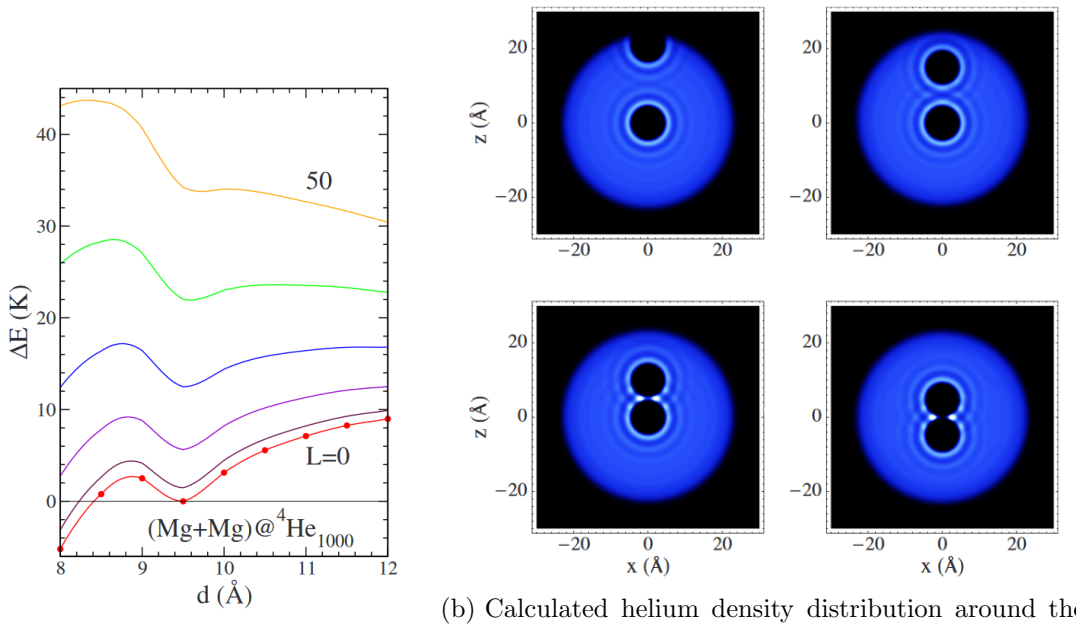

(a) Pair potential of the Mg-Mg distance for the symmetric configuration (Mg_2 center of mass in the droplet center) for different angular momenta L.

(b) Calculated helium density distribution around the two Mg atoms for interatomic distances of 18.5, 12.9 and 9.3 Å. The lower right image shows the density for the symmetric configuration at an interatomic distance of 9.5 Å. Bright regions mark large helium density.

Figure 1.3: Helium density functional theory results for the magnesium dimer inside a helium droplet with 1000 helium atoms. [8]

the monomer ejection time of 50 ps.

1.2.2 Dynamics of Magnesium

Single magnesium atoms are expected to show similar dynamics as indium atoms with respect to bubble expansion. The helium free bubble will form around the magnesium atoms. Due to the helium environment, two solvated magnesium atoms will not interact in the same way as they do in vacuum.

Helium Density Functional Theory (HeDFT) simulations [8] have suggested that the Mg-Mg pair potential inside the droplet has a local minimum at around 9.5 Å when the two Mg atoms are placed symmetrically inside the helium droplet (see Figure 1.3a). This minimum is separated from the global minimum at 3 Å by a potential barrier less than 1 meV. When the potential barrier is somehow overcome, the Mg dimer system will relax to the global minimum at 3 Å. The energy difference between the local and global minimum is transferred to the Mg nuclei and electrons as kinetic energy and electronic excitation respectively.

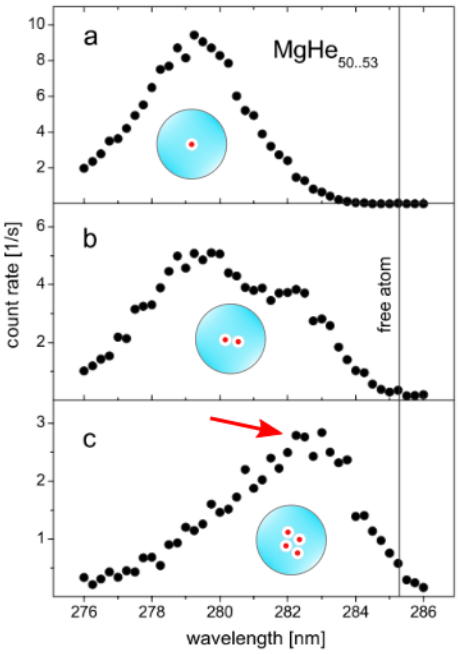

Figure 1.4: R2PI spectra for Mg^+ counts and different helium droplet ($\overline{N}_{He} = 6000$) doping conditions. top: $\overline{N}_{Mg} < 1$; middle: $\overline{N}_{Mg} = 2$; bottom: $\overline{N}_{Mg} = 4$. The peak at 282.5 nm (arrow) is the resonance wavelength of the magnesium foam.

1.2.3 Experimental Indicators for Mg Foam

R2PI, 800 nm Pump Probe, Ion Spectroscopy

Magnesium in helium droplets was previously studied using Resonant Two Photon Ionization (R2PI) in combination with ion detection [20]. A shift of the atomic absorption of magnesium from 279 nm to 282.5 nm was found (see Figure 1.4), which was caused by increasing the Mg doping level inside the helium droplets from $\overline{N}_{Mg} < 1$ to $\overline{N}_{Mg} \approx 4$ on average. This shift in absorption was also observed in [22]. Varying the droplet size did not influence the shift. To rule out simple dimer fragmentation as the source of this shift, the count rates on Mg mass channels up to Mg_{15} were observed, with the result that all cluster signals show this shift in absorption. This is a strong indication that the Mg atoms are the absorbing species, and that they form a metastable foam inside the helium droplet. Additionally, the appearance of a distinct peak in the absorption spectrum at 282.5 nm implies a preferred distance between the magnesium atoms, instead of a random distribution of Mg atoms. The random distribution would lead to a broadening of the peak to larger wavelengths corresponding to every possible Mg-Mg distance. The metastable binding of the He atoms can be intuitively described by overlapping and constructive interference of the helium density that surrounds the magnesium dopants (see Figure 1.5). This approach leads to an equilibrium interatomic distance of about 10 Å which is remarkably close to the HeDFT result.

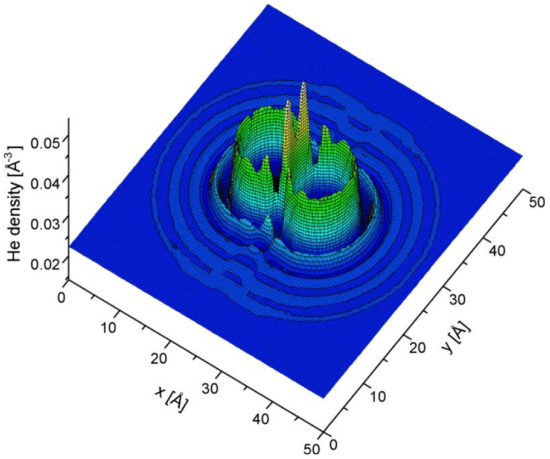

Figure 1.5: Simulation of helium density (obtained by overlapping density around one Mg atom) surrounding two magnesium atoms inside helium separated by 10 Å. The helium density is increased between the atoms. [20]

Strong Field 800 nm Pump-Probe, Ion Spectroscopy

More experimental data on the Mg-He system was obtained by performing a strong field pump-probe experiment with ion detection using a strong (intensity $I = 6 \times 10^{11}\mathrm{W/cm^2}$) and a weak ($I = 2 \times 10^{11}\mathrm{W/cm^2}$) pulse [Full Width at Half Maximum (FWHM) 200 fs, $\lambda =$ 800 nm]. As described by the Göde et. al. [4], the Mg atoms undergo photoexcitation by the pump pulse and multiphoton ionization by the probe pulse. An initial reduction of the ion signal shortly after the pump-probe pulse overlap was found (see Figure 1.6a). This reduction is attributed to a decrease in ionization crosssection of the collapsed cluster, caused by the change in bond character from nonmetallic to metallic during the collapse. A metallic cluster can relax much faster (on the order of fs), thus reducing the probability for multiphoton ionization. The subsequent signal recovery is attributed to exciplex ejection time out of the droplet (estimated to be around 50 ps).
Using the technique of colored double pulses (FWHM 60 fs, $\lambda = 800$ nm) the system response near zero time delay was measured. The first pulse ionizes the Mg foam and starts the collapse. During the collapse the resonance frequency of the system shifts toward higher frequencies, which reduces the ionization crosssection for the second pulse. The collapse is estimate to take about 350 fs (see Figure 1.6b). All ionic channels show the same decay time, which shows that the response does not originate from clusters but from the Mg foam. This is an important difference to the decay times of other metal clusters ($\approx$ 100 fs) which is size dependent.

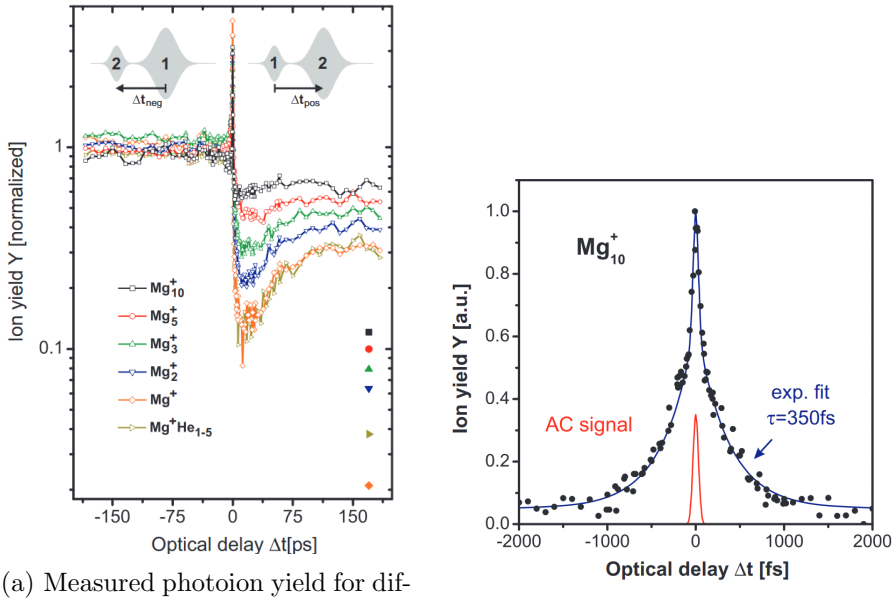

(a) Measured photoion yield for different magnesium cluster sizes and snowballs. (Mg^+He_N as a function of 800 nm pump-probe delay, with a weak leading pulse and a strong trailing pulse)

(b) Colored double pulse (FWHM 60 fs) measurement of the Mg_{10}^+ ion signal near zero optical delay. A decay time of 350 fs is determined and attributed to foam collapse.

Figure 1.6: Results of the 800 nm pump-probe measurements done by Przystawik et. al. [20].

R2PI Photoelectron Spectroscopy

In the most recent paper of the Rostock group [9], photoelectron spectroscopy was conducted in combination with R2PI at 282.5 nm. Figure 1.7a shows the photoelectron spectrum of free Mg atoms as well as of helium droplets with an average of 0.1 and 17 Mg atoms inside. The PE peak in the $\overline{N}_{Mg} = 0.1$ spectrum is shifted by about 0.1 eV to lower energies compared to the free Mg atom PE peak. A weak PE signal at low binding energies (large photoelectron energies, see Figure 1.7a), is visible. These high energy electrons originate from atomic levels that are not excitable using the 282.5 nm laser. Highly excited electronic states are populated during the foam collapse where about 1 eV of energy is released per magnesium atom.
Figure 1.7b shows R2PI photoelectron spectra as a function of average Mg doping. The foam related signal lies between 3 and 0.5 eV binding energy. The signal below 3 eV stems from free Mg and single Mg inside the helium. Photoelectrons with binding energies larger than 3.5 eV are associated with Mg exciplexes. Cluster fragments do not contribute to the signal. A lower and upper bound on the Mg doping level was determined within which the foam signatures can be observed. The lower bound stems from the fact that a minimum of 2 eV must be released in the collapse for the highly excited states to be populated. N_{min} is different for electronic states with different energy, for example photoelectrons with 1 to 1.5 eV energy in Figure 1.7b are only detected for average Mg doping greater than 10 Mg atoms.

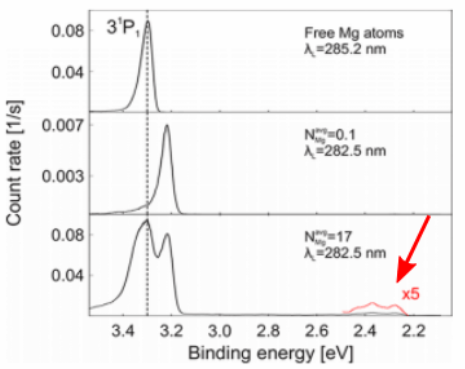

(a)

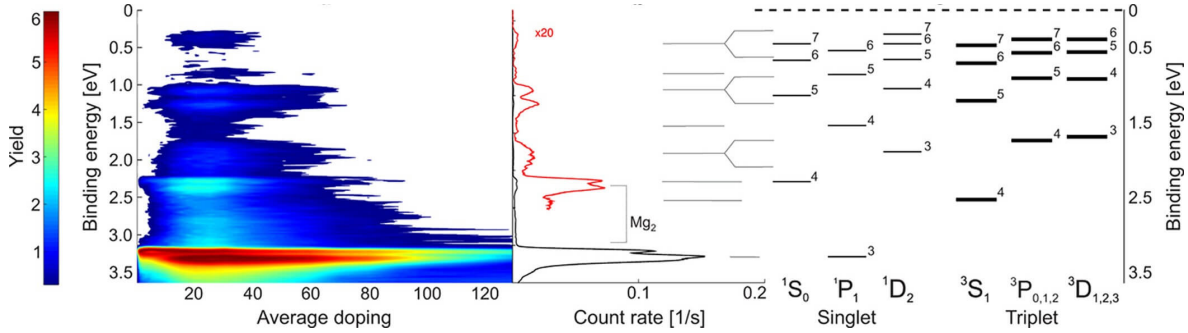

(b)

Figure 1.7: Results of the R2PI photoelectron spectroscopy measurements. (a) Photoelectron spectra of free Mg, single Mg in helium droplet and on average 17 Mg atoms in helium droplet. The electrons with low binding energies (arrow) are associated with Mg foam collapse. (b) R2PI photoelectron spectra recorded for different Mg doping levels (left). The peaks do not shift as the number of Mg atoms inside the helium droplets ($\overline{N}_{He} = 5.2 \times 10^4$) is increased. For reference the term diagram of Mg (right) as well as a PE spectrum at ($\overline{N}_{Mg} = 30$) is shown (center). [9]

If there are many Mg atoms present inside the helium droplet the foam becomes unstable and collapses spontaneously before reaching the laser and molecular beam interaction region. This spontaneous collapse is the reason for the upper Mg doping bound above which no high energy electrons are detected. Figure 1.8 shows the upper and lower bound for $\overline{N}_{Mg}$ as a function of the mean helium droplet radius.

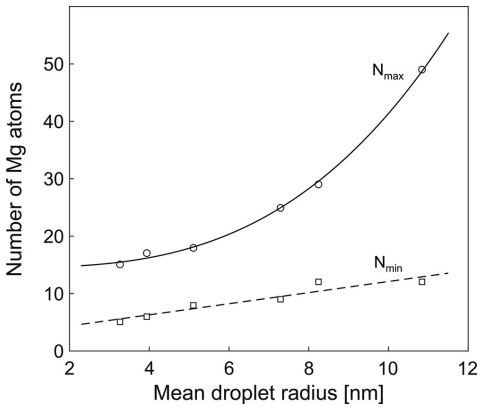

Figure 1.8: Minimum and maximum number of Mg atoms required to be present inside the helium droplet in order to observe PE signals related to the foam collapse, plotted over mean helium droplet radius. [9]

Chapter 2

Experimental

He_N droplets were generated by supersonic expansion through a cold nozzle (temperature T_0 between 11 K and 15 K, 5 μm nozzle diameter). The helium undergoes a phase transition to the superfluid phase and condensates into droplets. The size of the droplets after the expansion is controlled by the temperature T_0 of the nozzle. By evaporation of helium atoms the droplets can reach temperatures as low as 0.37 K. More information about helium droplets and their applications in spectroscopy can be found in [28] and [15].
Resistively heated ovens were used to evaporate magnesium metal. The droplets pass through the metal vapor and pick up some magnesium atoms. The number of magnesium atoms inside the droplets was characterized using a Quadrupol Mass Spectrometer (QMS). QMS currents were recorded for the Mg mass (24 u) and multiples of the Mg mass at a range of pickup currents (current $\propto$ Mg vapor pressure). The resulting pickup curves can be viewed in Appendix section B.
The magnesium atoms were excited near the foam resonance (282.5 nm, see Figure 1.4) and ionized using a pump-probe pulse scheme (λ_{pump} = 282.6 nm with 3.6 nm FWHM; λ_{probe} = 400 nm with 8.6 nm FWHM / 272 nm with 3.5 nm FWHM). Pulse energies were in the range of μJ. Laser pulse durations of about 50 fs were used. The pulse durations were not measured directly but were estimated from the detected crosscorrelation signal (see Figure 3.2). Ionization products were detected using a Time of Flight (ToF) spectrometer. Flight times were translated into energy spectra for electrons and mass spectra for ions.
Most of the experimental setup was already present at the start of the thesis and previous master students have documented the setup in detail. A comprehensive list which shows where to find information about which part of the experimental setup is given in Table 2.1 .

2.1 Setup

The experimental setup consists of the vacuum system and the laser system. The vacuum system is subdivided into three parts. The source chamber, where the helium droplets are formed, the pick up chamber where the droplets pick up dopant atoms and the main chamber where the doped droplets interact with the pump and probe laser pulses (see Figure 2.1).

Table 2.1: Documentation of the experimental setup by previous master students.

Year	Author	Part of Setup	Reference
2016	M. Bainschab	magnetic bottle	[2]
2017	B. Thaler	SHG pump-probe, ToF data acquisition	[24]
2017	P. Heim	finding pump-probe overlap	[6]
2017	S. Ranftl	resistively heated oven control vacuum system	[21]
2018	S. Cesnik	optical parametric amplifier laboratory oversight server	[3]

The main chamber also houses the ToF spectrometer and the QMS. The vacuum inside the chambers is maintained by two prevacuum scroll pumps and four turbomolecular pumps.

2.1.1 Source Chamber and Droplet Formation

In the source chamber the formation of liquid helium (^{4}He) droplets takes place. The helium is precooled at the cold head at a pressure of 20 to 40 bar. The gas is then expanded through a nozzle with 5 μm diameter. The expansion happens sub-critically. The droplet sizes follow a log-normal distribution, and the mean droplet size follows a scaling law (Knuth model). Both the distribution of sizes and the mean size are dependent on the source temperature T_0 and helium source pressure. For very high pressures and low temperatures the helium liquefies before leaving the nozzle (see Figure 2.2b), which leads to the formation of very large droplets. However, with the equipment used in this work, this regime could not be reached.
For a fixed pressure, the mean size gets smaller with increasing temperature. At a fixed temperature, higher pressures lead to the formation of larger droplets. [12]
The background pressure in the source chamber can also influence the droplet sizes. A larger background pressure raises the minimum nozzle temperature by enabling more heat to be transferred to the nozzle through convection. The increased nozzle temperature then decreases the droplet size. A large background pressure may also prevent the formation of droplets entirely, because it can lead to the formation of shock waves close to the nozzle.
Droplet sizes in this work are determined by approximately reading off the value from Figure 2.2c. The droplet radius R_0 is related to the number of helium atoms N by

$$R_0 = 2.22\ N^{1/3}\ \text{Å}$$

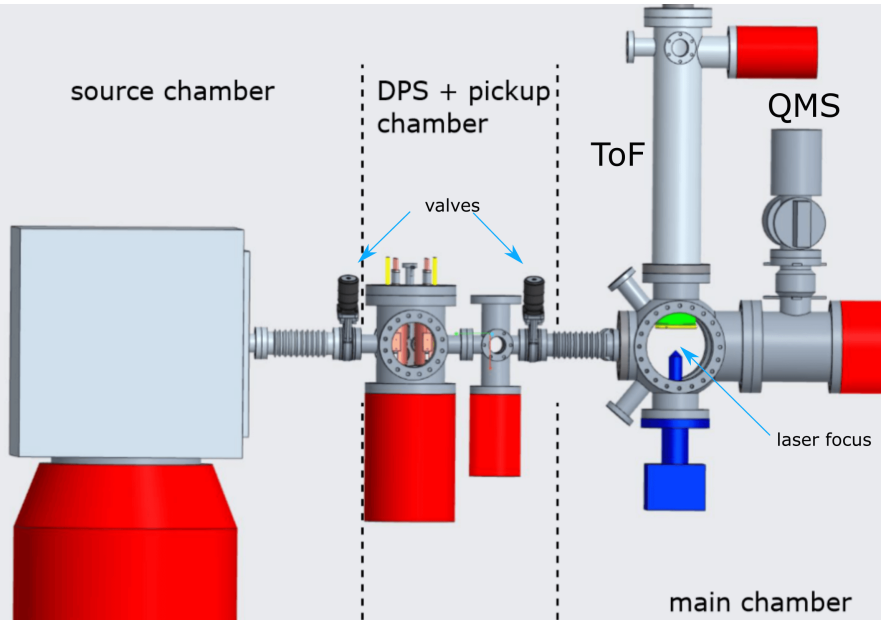

Figure 2.1: CAD drawing of the vacuum chamber assembly. [25] ToF: time-of-flight spectrometer, QMS: quadrupol mass spectrometer, DPS: differential pumping stage.

A skimmer is used to extract the helium droplets from the source chamber. The distance between nozzle and skimmer influences the amount of helium extracted from the source chamber (see Appendix section A.1).

For monitoring purposes the status of the source chamber turbomolecular pump can be read out using the pumps RS232 protocol on the service connector. A python class is used to facilitate the readout and relay the information to the laboratory oversight website. The python code for this class is described in the Appendix Listing C.1.

Supersonic Expansion

The helium droplets are created by supersonic expansion (also called free jet expansion) of helium gas through a small diameter (5 μm) nozzle. The helium has temperature T_0 and pressure p_0 before the expansion. The expansion can be described in two complementary ways, by using thermodynamics and fluid dynamics.
Close to the nozzle, the mean free path of the helium atoms is very small due to the high pressure [1]. This means that the interaction between the atoms is strong. An ensemble of strongly interacting particles can reach thermodynamic equilibrium very quickly, thus the expansion is reversible. The system is at equilibrium at each point in time during the first moments of the expansion. Additionally, no heat is exchanged with the environment, since the source chamber pressure further away from the expansion region is very small (there are

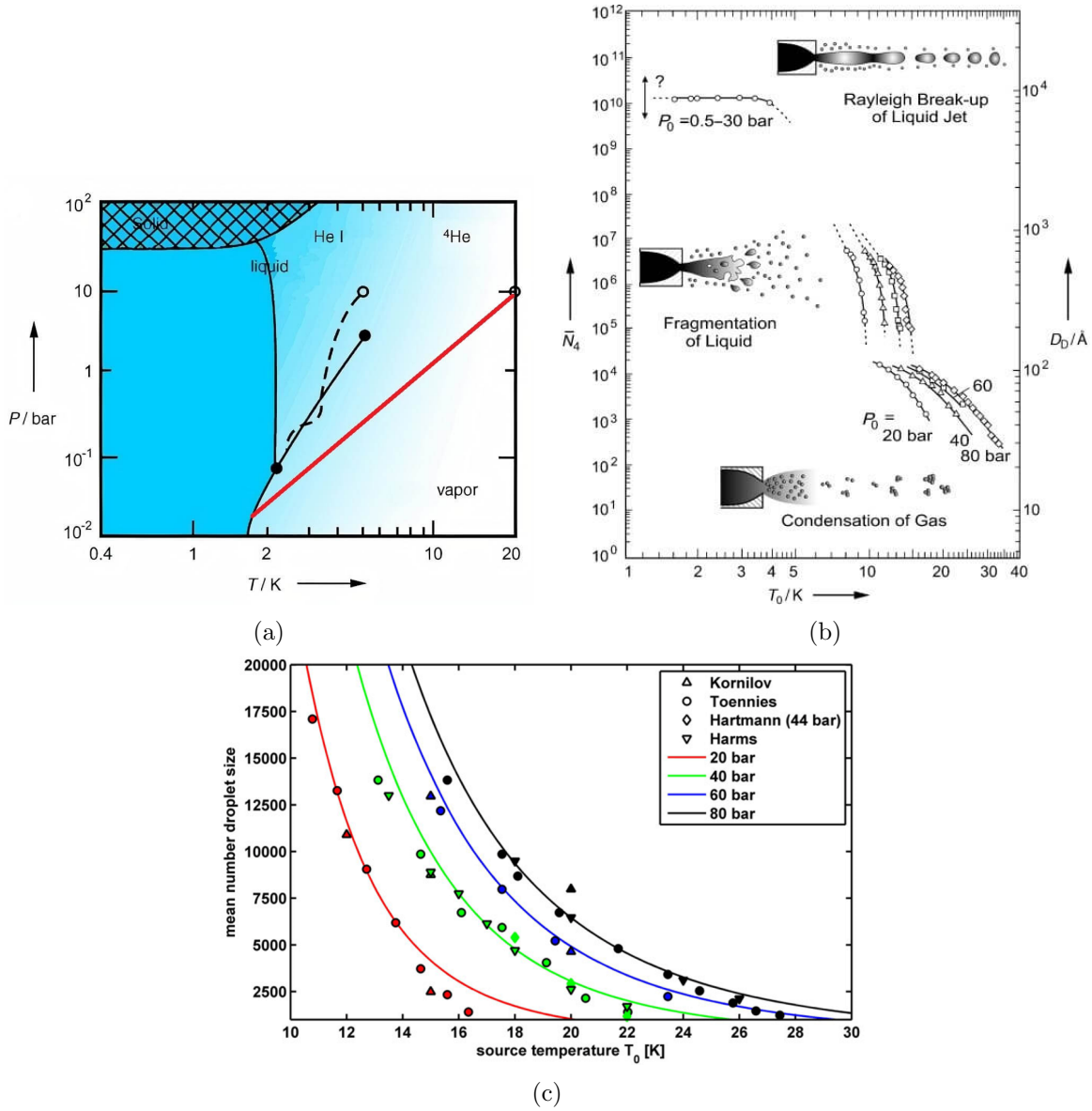

Figure 2.2: (a) Phase diagram of ^{4}He, the red line shows the phase transition which occurs during the supersonic expansion (b) Mean number of helium atoms in the droplet ($\overline{N}_4$) as a function of helium source pressure P_0 and nozzle temperature T_0. Three distinct jet operation modes are shown. In this thesis, the pressure was 20 or 40 bar at a minimum of 11 K source temperature, which is part of the sub-critical curves on the lower right of the diagram. [28] (c) Compilation of experimentally determined mean droplet sizes, from [12]. The curves in (c) were used to give values for the droplet sizes in this work.

no other particles available which could take heat from the helium atoms). Therefore, the expansion is adiabatic, and the system enthalpy stays constant during the expansion.
In a simplified model of the expansion (see [5]), the gas is assumed to be ideal. Before the expansion the gas inside the cold head has the enthalpy $H_0 = c_p T_0$ with pressure p_0 and temperature T_0 . After the expansion, some of the enthalpy has been converted into kinetic energy $mu^2/2$ of the directed flow with velocity u out of the nozzle. The requirement for enthalpy to remain constant leads to the following expression:

$$H_0 = c_p T_0 = H + mu^2/2 \tag{2.1}$$

Along a streamline in the expansion a local temperature T can be defined. Using equation (2.1) the enthalpy conservation along a streamline is:

$$c_p T_0 = c_p T + mu^2/2 \tag{2.2}$$

Using the relations $k_B = c_p - c_v$ and $\gamma = c_p/c_v$ one can derive an implicit equation for the temperature along a steamline:

$$\begin{aligned} T = T_0 \left[1 + 1/2(\gamma - 1)M(T)^2\right]^{-1} \\ M(T) = u/c(T) \\ c(T) = (\gamma k_B T/m)^{1/2} \end{aligned} \tag{2.3}$$

Here M is the local Mach number and c is the local speed of sound. The local Mach number is enough to completely characterize the thermodynamic properties along the streamline, since pressure and density can be obtained from entropy conservation [Poisson equations of adiabatic expansion, see equation (2.4)].

$$\frac{p}{p_0} = \left(\frac{\rho}{\rho_0}\right)^{\gamma} = \left(\frac{T}{T_0}\right)^{\gamma/(\gamma-1)} \tag{2.4}$$

The local Mach number M must be obtained by solving the partial differential equation for isentropic, compressible flow. When the Mach number gets large the velocity distribution of the gas becomes very narrow.
The evolution of the Mach number is described below. A detailed description of the free jet expansion and the formation of shockwave structures is given in [19].
The gas is accelerated proportional to the reduction of the nozzle diameter. At the nozzle exit $M = 1$ is reached. If the pressure ratio p_0/p_a is above some critical value, the local pressure of the gas is larger than the ambient pressure p_a inside the source chamber, and is said to be under-expanded. The gas will expand further after exiting the nozzle to meet the boundary condition pressure of p_a. The Mach number increases with increasing distance to the nozzle. When the ambient pressure p_a is high, boundary conditions will recompress the

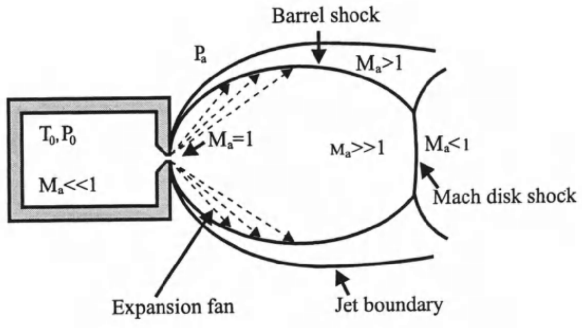

Figure 2.3: Schematic of the free jet expansion, taken from [19]

gas which leads to the formation of a shock wave structure, to the side (barrel shock) and the forward direction (Mach disk) (see Figure 2.3). This could for example happen when some obstacle is moved very close to the nozzle exit.
Inside the shock wave structure (i. e. the region where the gas moves faster than the local speed of sound) the gas is not influenced by the surrounding source chamber gas. This region is called “zone of silence”. The helium is extracted from this region by the skimmer, which has a special conical shape (see Figure C.2) in order to minimize its influence on the expansion process.
The continuum mechanic description of the expansion relies on some minimum density of the particles to be applicable. Far away from the nozzle the mean free path becomes large, which means the particle interactions become rare. Due to the lack of collisions the continuum properties are ”frozen in”. Due to the narrow velocity distribution of the helium atoms in the beam direction, the helium atoms condensate and form superfluid droplets.

2.1.2 Pickup Chamber

In the pickup chamber the superfluid droplets are doped using metal vapor. The metal is contained in a resistively heated ceramic oven. The oven temperature and therefore the metal vapor pressure is set using a fixed current. A direct temperature measurement of the metal is difficult, because the thermocouple is attached to the outside of the ceramic oven. The temperature of the oven does not match the temperature of the metal.
The droplets pass through the metal vapor and pick up a varying number of dopant atoms. The number of atoms which are picked up depends on the droplet size and the vapor pressure inside the pickup chamber. A good approximation for the pickup cross section ($\propto$ pickup probability) is the geometric cross section of the helium droplets. It is equal to the area of a circle with the droplet radius R_o [12]. The pickup crosssection σ [equation (2.5)] therefore

depends on the droplet size N and the number of dopant atoms k.

$$\begin{aligned} \sigma(N) &= \pi R_0(N)^2 \\ N &= N(k) \end{aligned} \tag{2.5}$$

After a dopant atom has entered the helium droplet its kinetic energy is transferred to the helium atoms. This transfer leads to the evaporation of some helium atoms. The evaporation introduces a k dependence to the number of helium atoms N in the droplet. For single atom pickup this dependence is negligible, however when a large number of dopant atoms enters the droplet the k dependence becomes an important factor for the pickup process. For very high doping the helium droplet can evaporate away completely.
The probability for a droplet of size N to pick up k dopant atoms has been shown to be Poisson distributed [see equation (2.6)].

$$p(k|\sigma, \rho, L) = \frac{(\sigma\rho L)^k}{!k} e^{-\sigma\rho L} \tag{2.6}$$

Here, ρ is the dopant density inside the pickup cell and L is the length of the cell.
Currently, no direct way of measuring the density of the dopant gas inside the pick-up ovens is available, due to the complicated pick-up cell geometry and difficulty in determining the oven temperature. This means that it is not possible to give an accurate value for the number of Mg atoms picked up for fixed pickup conditions and droplet sizes. Only a rough estimate based on the most prominent Mg cluster size at some oven current measured by the QMS can be given (see Appendix section B).

2.1.3 Differential Pumping Stage

In order to improve the main chamber vacuum a Differential Pumping Stage (DPS) separates the main chamber and the pickup chamber. Effusive gas background is greatly reduced by this design, because helium and dopant gas, which is not part of the helium beam, is pumped off.

2.1.4 Main chamber

The doped helium droplets leave the pickup chamber / DPS and enter the main chamber. Once the droplets pass over the repeller and through the laser beam focus, ions and free electrons are generated. The charges are detected by the magnetic bottle time-of-flight spectrometer. The magnetic bottle consists of permanent magnet on the repeller in combination with a large solenoid wrapped around the inside of the time-of-flight tube. The magnetic bottle serves to increase electron detection efficiency [11]. The voltage on the repeller and the repeller position can be varied to achieve optimal energy resolution. For electron detection a

small negative voltage is applied to the repeller (up to 5 V) and for ion detection a large positive voltage is applied. The repeller can also be translated in the plane parallel to the laser table to move it below the laser focus. After passing through the laser focus, the molecular beam enters the ionization region of the quadrupole mass spectrometer. The QMS is used to analyze which atoms and molecules are present in the molecular beam. This can be done for different oven currents resulting in the pickup curves shown in Figure B.1.

2.1.5 Time-of-Flight Spectrometer

The time-of-flight spectrometer enables the measurement of electron energies and ion masses. It is described in detail in [2]. The charged particles are accelerated toward the multichannel plate, where they are detected as voltage pulses. When a pulse is measured, its arrival time relative to the laser trigger signal is saved. The count events are then converted into a histogram of counts over time-of-flight. The time-of-flight histogram is then transformed into an energy spectrum for electrons and a mass spectrum for ions (the matlab code for this transformation is described in [24]).
The energy resolution of the ToF spectrometer is limited by the magnetic bottle ($\Delta E/E \approx 4\%$) and the bandwidth of the laser pulses used. For one photon excitation by the pump pulse (FWHM $\Delta\nu_{pump}$) and one photon ionization by the probe pulse (FWHM $\Delta\nu_{probe}$) the energy resolution is given by:

$$\Delta E = \sqrt{(0.04E)^2 + (h\Delta\nu_{pump})^2 + (h\Delta\nu_{probe})^2} \tag{2.7}$$

where h is the planck constant [2].
For example, at 3 eV photoelectron energy as well as $\Delta\nu_{pump} = 13.15$ THz (282.5 nm, FWHM 3.5 nm) and $\Delta\nu_{probe} = 16.86$ THz (400 nm, FWHM 9 nm) the energy resolution is about 5%. At higher photoelectron energies the resolution becomes worse.

2.1.6 Optical Setup

The femtosecond pulses needed for the time resolved measurements are generated at a repetition rate of 3 kHz by a Ti:Sapphire laser (Vitara Coherent) and amplified using a chirped pulse amplification system (Legend Elite Duo, Evolution generates pump beam) [24]. The laser power at the output is 12.6 W and the polarization direction is normal to the laser table plane. The spectral distribution of the laser pulses is centered at 800 nm with a bandwidth of 60 nm. The laser setup is shown schematically in Figure 2.4. After the Legend output the laser beam is split using a beam splitter (BS). The more intense beam (80 % intensity) is used inside the Optical Parametric Amplifier (OPA), of type Coherent OPerA Solo, where the 800 nm pulse is converted to the desired excitation wavelength of 282.5 nm. The power of the OPA pulse can be reduced using a wire grid polarizer.

The less intense beam (20 % intensity) is guided through a compensation path (see Figure 2.5), an adjustable $\lambda/2$ plate and two brewster windows (pulse power control), a telescope (optional), the computer controlled delay stage and a Second Harmonic Generation (SHG) crystal. After the SHG crystal a Time Delay Compensator (TDC) another $\lambda/2$ plate and a Sum Frequency Mixing (SFM) crystal can be inserted to generate 266 nm pulses. Dichroic mirrors are used to remove unwanted residual light from the fundamental (800 nm).
Both beams are focused inside the main chamber above the repeller with a f = 100 cm lens. Two arduino controlled shutters are used to block out pump and probe beams. Pump-probe spectra are obtained by subtracting the pump-only and probe-only contributions from the combined pump + probe signal.
Spacial overlap of the pump and probe beams is adjusted using a beam profiler and a flip mirror in front of the main chamber entrance window. Temporal overlap is roughly measured with a photodiode and an oscilloscope, and adjusted using a stage in the OPA compensation path. The fine overlap adjustment is usually done by exciting some dopant inside the He droplets (for example Mg at 285.5 nm) and ionizing with the probe pulse. Near the temporal overlap (= zero time delay point) the ionization probability is greatly enhanced. By comparing the detected electron counts of the sum of pump-only and probe-only signals to the pump+probe signal one can identify the zero time delay point.
Using very intense pump and probe pulses one can use an effusive gas to determine the time zero point directly. When the pulses overlap, the nonresonant ionization probability is higher compared to when they do not overlap. This can be seen in the total photoelectron signal over time delay as a gaussian peak.

Wavelength Selection

The optical parametric amplifier is used to generate laser pulses with the desired spectrum from the 800 nm pump pulse. The pump beam is split into signal and idler beam, satisfying energy and momentum conservation [3] ($\hbar\omega$ is the photon energy).

$$\begin{aligned} \hbar\omega_{pump} &= \hbar\omega_{signal} + \hbar\omega_{idler} \\ \hbar k(\omega_{pump}) &= \hbar k(\omega_{signal}) + \hbar k(\omega_{idler}) \end{aligned} \tag{2.8}$$

The signal, idler and pump beams can then be doubled, and / or mixed using nonlinear crystals to arrive at the required output spectrum.
A more direct method of wavelength selection is to use second and third harmonic generation of the 800 nm pulse. To accomplish this wavelength selection nonlinear crystals are used. In the case of second harmonic generation one SHG crystal [Barium Borate (BBO) with 200 μm thickness] is used.
In order to produce 266 nm pulses additional components are needed. After the SHG crystal

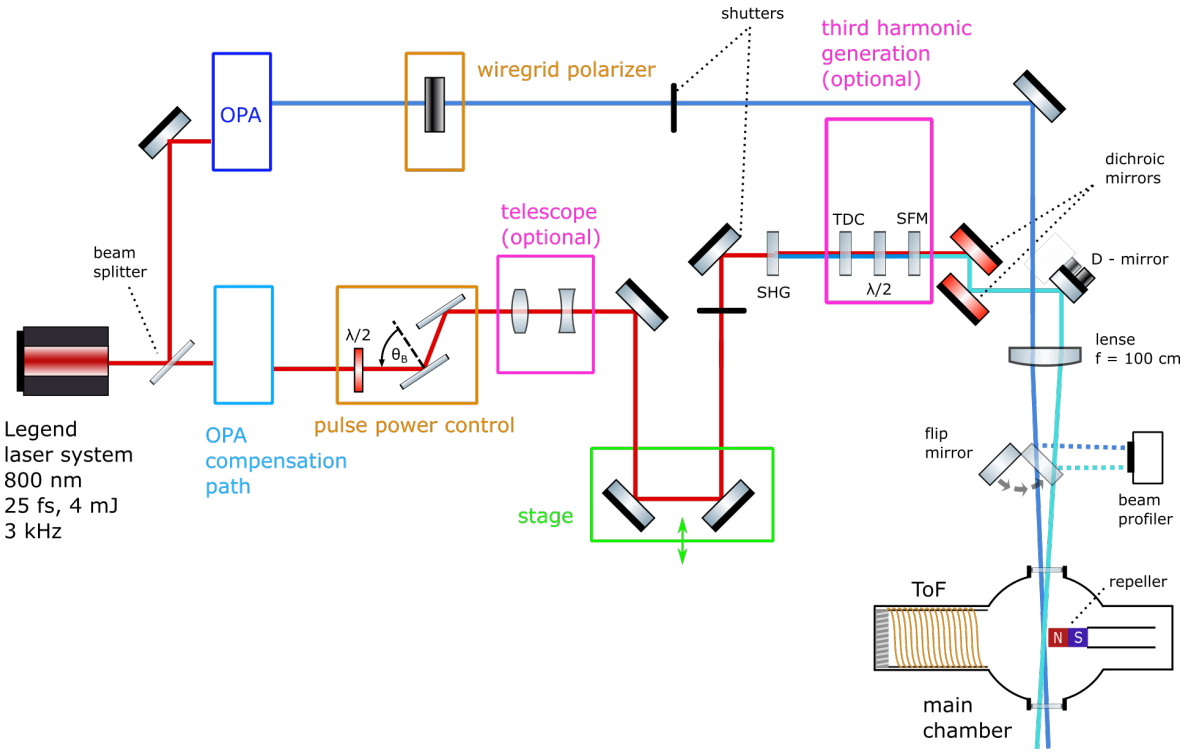

Figure 2.4: Schematic of the laser setup used for pump probe measurements. OPA: optical parametric amplifier, SHG: second harmonic generator crystal, TDC: time delay compensator, SFM: sum frequency mixing crystal, ToF: time-of-flight spectrometer.

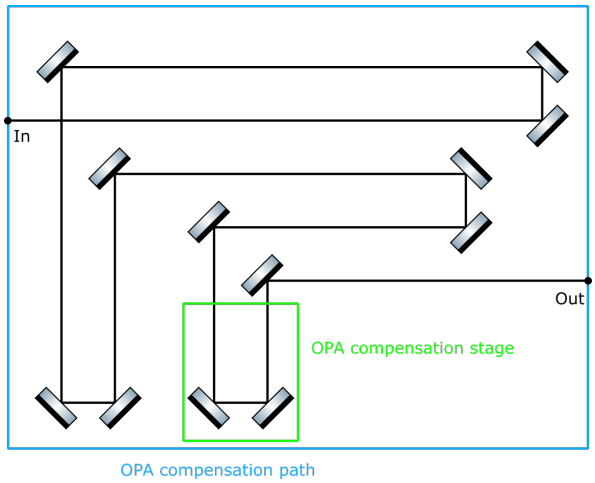

Figure 2.5: Schematic of the optical parametric amplifier (OPA) compensation path. The laser path was constructed in this folded way to minimize the laser table area needed. The OPA compensation stage is used to correct large timing offsets of the OPA pulse and the stage pulse.

(BBO, 200 μm) a 400 nm pulse with horizontal polarization and a 800 nm residual pulse with vertical polarization are present. Because of normal dispersion inside the SHG crystal the 400 nm pulse is delayed with respect to the 800 nm pulse. A time delay compensator (TDC, calcite) is used to correct this. The TDC has different indices of refraction along its ordinary and extraordinary axis. Since the phase velocity is given by $v_p = c/n$ the 400 nm pulse can be made "faster" than the 800 nm pulse by rotating the TDC.
After the time delay has been compensated, the polarization of the 800 nm pulse is rotated using a $\lambda/2$ plate so that it is parallel to the polarization of the 400 nm pulse. This is needed for sum frequency mixing in the next nonlinear crystal. The SFM crystal (BBO, 200 μm) produces 266 nm pulses by combining one 800 nm photon and one 400 nm photon. Tilt and rotation of all four optical components needed for Third Harmonic Generation (THG) are optimized with respect to output power and spectral distribution. The THG power is monitored using a power meter after two dichroic mirrors and a spectrometer.
The tilt of the SHG and SFM crystals can also be used to change the phase matching condition which enables the choice of center wavelength of the THG pulse.

2.2 Photoelectron and Ion Signal Fitting

2.2.1 Exponential Decay

In order to obtain characteristic decay times τ from the photoelectron and ion timescan data, the time dependent signals $S(t)$ (electron and ion counts per second over pump-probe time delay) are fitted with an exponential decay function [see equation (2.9)] when appropriate. The t_0 parameter marks the start time of the decay, and was chosen to be the time where the fitted curves are at their maximum.

$$S(t) = ae^{-(t-t_0)/\tau} + c \tag{2.9}$$

2.2.2 Two Level Population

The time dependent photoelectron and ion counts can also be fitted with a population function of a two level system (excited state and ground state).
The signals at some time delay between pump and probe pulse are proportional to the population of some excited state of the system. The population is filled by a gaussian pulse $g(t)$ (pump pulse) with standard deviation σ and mean t_0, and decays with a time constant τ from the excited state to the ground state, see equation (2.10). The parameter t_0 marks the point of zero time delay. Any deviation of this parameter from zero points to a delayed start of the observed signal.

$$\dot{N}(t) = -N/\tau + g(t) \tag{2.10}$$

Equation 2.10 is solved by using the fact that a solution to this equation with the source term $g(t)$ is the convolution of the greens function $G(t)$ of this differential equation with the source term [6], see equation (2.11).

$$\begin{aligned} G(t) &= \theta(t)e^{-t/\tau} \\ N(t) &= \int_{-\infty}^{\infty} \mathrm{d}t'\, G(t-t')g(t') \\ g(t) &= ae^{-(t-t_0)^2/(2\sigma^2)} \end{aligned} \tag{2.11}$$

The resulting population over time $N(t)$ is given by equation (2.12), where a is a free amplitude parameter and c is a constant background.

$$\begin{aligned} N(t) = ae^{-t/\tau}\left[2 - \mathrm{erfc}\left((t-b)/(\sqrt{2}\sigma)\right)\right] + c \\ b = \sigma^2/\tau + t_0 \end{aligned} \tag{2.12}$$

2.3 Magnesium Energy Levels and Pulse Center Wavelengths

For convenience Table 2.2 shows the relevant Mg energy levels which are often mentioned in this work, and Table 2.3 shows typical pulse center wavelengths in multiple units and together with the corresponding spectral bandwidths (FWHM). The spectral bandwidth has to be taken into consideration when adjusting the pulse center wavelengths to match resonances.

Table 2.2: Atomic Mg energy levels in three different units [18]

Electron Configuration	Term	J	Level / cm^{-1}	Level / eV	Level / nm	Abbreviation
$3s^2$	^1S	0	0	0	0	Ground State (GS)
$3s3p$	$^1P^0$	1	35051.24	4.346	285.3	Excited State (ES)
Mg II ($^2S_{1/2}$)	limit		61671.09	7.646	162.15	Ionization Potential (IP)

Table 2.3: Typical pulse center wavelengths used in this work in multiple units. The spectral bandwidth (FWHM) in nm ($\Delta\lambda$) and eV (ΔE) is also given.

λ / nm	E / eV	f/ THz	ν / cm^{-1}	$\Delta\lambda$/ nm	ΔE / eV
282.5	4.389	1061.2	35398	3.5	0.054
272	4.558	1102.2	36765	3.5	0.054
266	4.661	1127.0	37594	3.4	0.060
400	3.100	749.48	25000	8.5	0.066

Chapter 3

Results

The results section is organized into two main parts corresponding to doping of the helium droplets with a large number of Mg atoms and doping with smaller number of Mg atoms. For each pump and probe pulse center wavelength photoelectron and ion spectra over pump-probe time delay are presented. The most important experimental parameters are given whenever they change between sections.

3.1 High Doping Concentration

3.1.1 282.6 nm pump, 400 nm probe

Experimental Parameters

Photoelectron and ion spectra in the timespan of -0.5 ps to 15 ps were measured. The pump pulse center wavelength was 282.6 nm (FWHM 3.4 nm) and the probe pulse center wavelength was 400.0 nm (FWHM 8.5 nm). The energies of these pulses are 4.39 eV and 3.10 eV respectively. The energy for the probe pulse was chosen because it avoids one-photon ionization from the magnesium excited state (ES, see Table 2.2) created by the pump pulse. This makes the resulting spectra near zero time delay easier to interpret.
A source pressure of 20 bar and a source temperature of 11 K were used, corresponding roughly to a mean droplet He number of $\overline{N} = 17500$ (see Figure 2.2c). All measurements in this subsection were performed in the multi-atom pickup regime.

Photoelectron Signals

For the PE timescans presented here, two sequential timescans were averaged to reduce noise. The energy averaged PE timescan in Figure 3.1a shows a rapid rise of the integrated photoelectron signal, followed by a decay. Most of the signal stems from photoelectrons with energies between 0.2 eV and 2.9 eV [signature (1) in Figures 3.1 and 3.2]. The binding energy of those electrons (E_{kin} - E_{probe}) is about 0.6 eV to 2.9 eV, which is similar to the energy of

the high energy electrons measured by the Rostock group in Figure 1.7a [9]. Interestingly, the signal between 1 and 2.9 eV (yellow transients in Figures 3.1 and 3.2) shows a fast initial decay before it rises again to a local maximum at $\sim$ 1 ps. Furthermore, a band at about 3.1 eV develops, with its maximum at 0.5 ps delay (2) and a delayed rise compared to the total integrated signal. A weak signal between 4 and 6 eV is also present [signature (3) in Figures 3.1 and 3.2]. After about 2 ps most of the PE signal has decayed (Figure 3.1b).
The PE signal between 0 and 0.2 eV PE energy shows a delayed rise after 7 ps [signature (4) in Figure 3.1b]. Also noteworthy is the bleach signal at about 1 eV which seems to become more prominent at later time delays [signature (5) in Figure 3.1b].

In Figure 3.2 the timescan from Figure 3.1b is compared with the effusive Mg cross correlation signal (dark red line, lower subplot), which was used to determine the zero time delay point. The band at about 4.7 eV (3) appears to have the same width in time as the effusive Mg signal, indicating that it stems from the crosscorrelation of the two laser pulses [1]. The 4.7 eV band can therefore be used as a marker for the zero time delay point. The center of the rising flank of band (1) containing the PE energy intervals 0.2 to 1 eV and 1 to 2.9 eV lies approximately at the 4.7 eV signal maximum (see Figure 3.1a) indicating that it originates from the excited state population increase caused by the pump pulse.

PE Signal Fitting

In order to analyze which energy signatures might have the same origin, the curves for different energy intervals were fitted with a two level population model and a simple exponential decay model (see Experimental section 2.2 for details concerning the fitting). All relevant fit parameters and their errors can be found in Tables 3.1 and 3.2.
The two level fit model assigns a zero time delay point of about 0.5 ps to all bands. The time zero point estimated by the model is thus off by about 500 fs. The discrepancy probably stems from only using a two level system as the model. In reality at least three energy levels might be present. The pulse length parameter σ was estimated to be about between 0.1 to 0.2 ps, except for the 1 to 2.9 eV band. This discrepancy stems from the delayed rise in the 2.9 eV band which led to a bad fit for this band.
The characteristic decay times obtained with an exponential decay fit for the PE signals range from 1.2 to 4.5 ps. The 1 to 2.9 eV band has the largest characteristic decay time with about 4.5 ps, which is about twice as long as all other decay times.
For the two level fit function the coupling between fit parameters b and t_0 most likely introduces large error between the parameters. The characteristic decay time τ has no coupling to the other parameters and might therefore give reasonable results.

[1] The maximum of the effusive signal is shifted in the positive delay direction by 15 fs. This is most likely due to backlash of the delay stage.

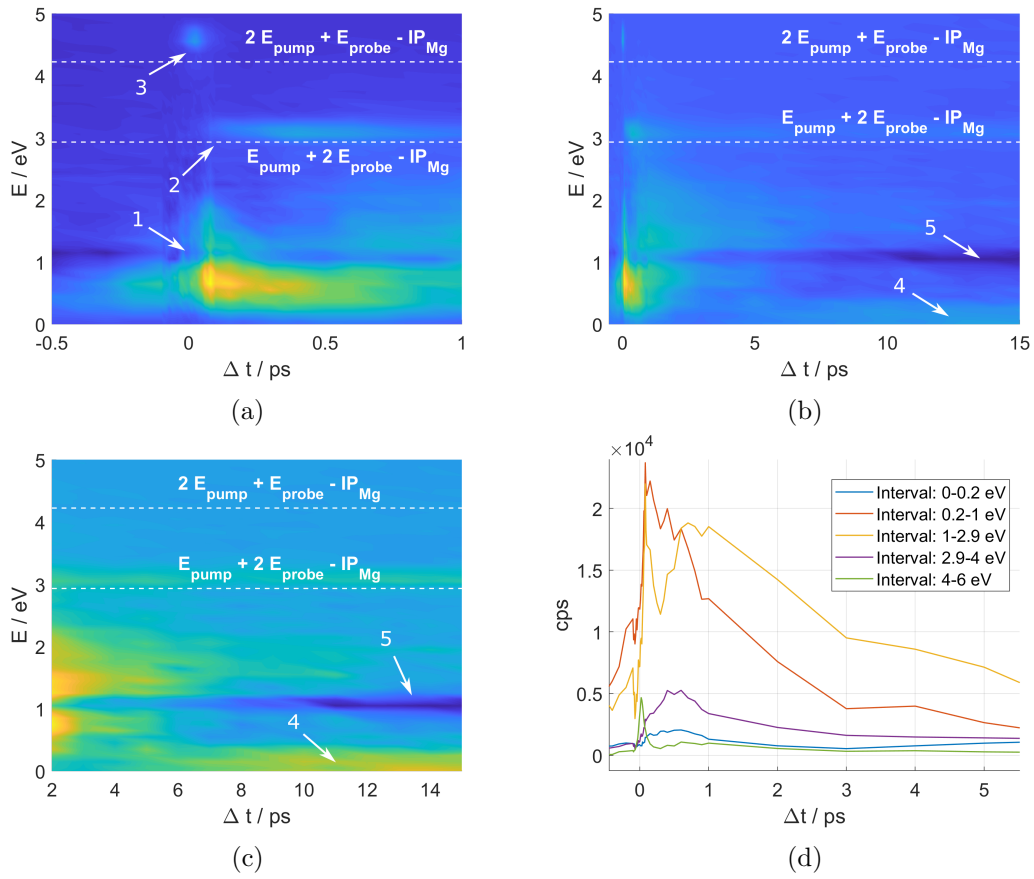

Figure 3.1: Three sections of the same PE timescan at high Mg doping conditions, white lines mark PE energies for three photon ionization of free Mg (see Figure 3.5)
(a) closeup near zero time delay (b) entire time delay range (c) long time delay range (d) integrated PE signals. $\lambda_{pump} = 282.6$ nm, $\lambda_{probe} = 400.6$ nm 08.07.20

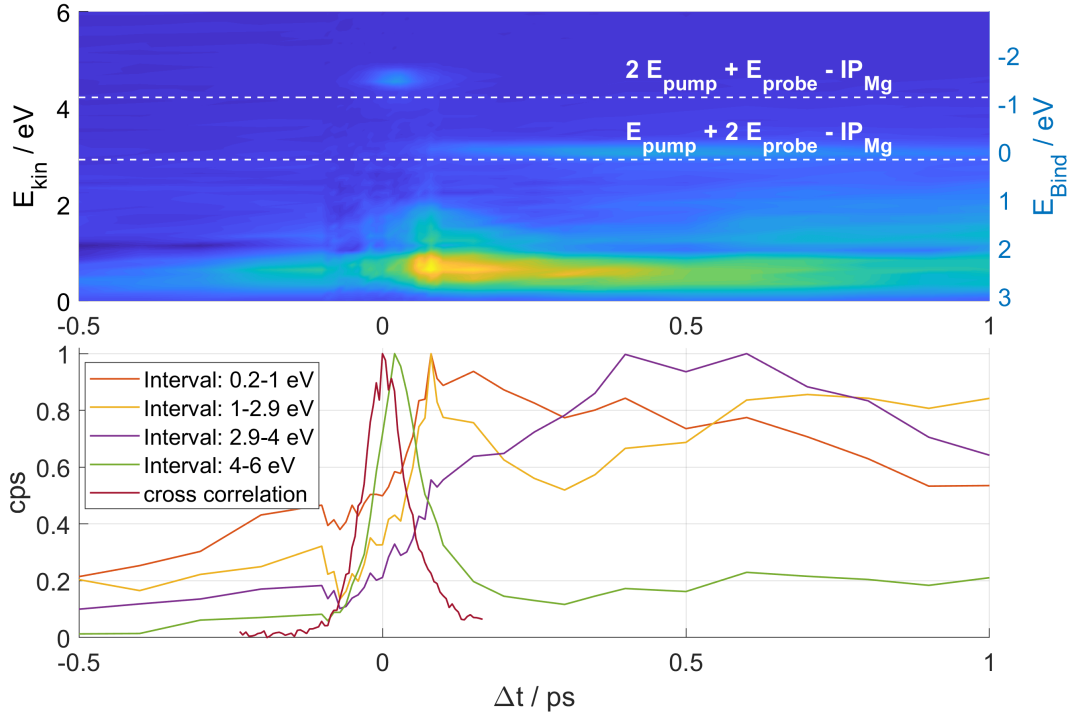

Figure 3.2: PE spectra timescan at high Mg doping conditions near zero time delay, the dark red line shows the effusive Mg crosscorrelation signal. $\lambda_{pump} = 282.6$ nm, $\lambda_{probe} = 400.6$ nm 08.07.20

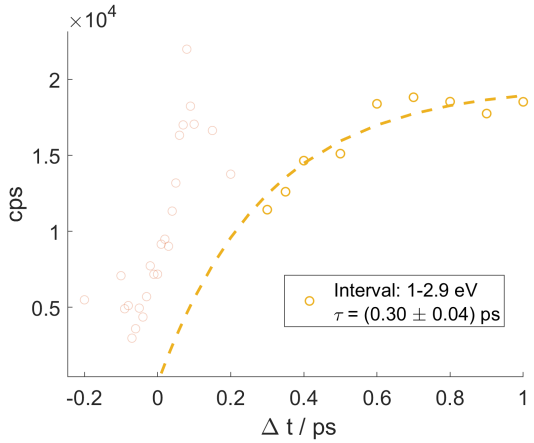

Figure 3.3: Exponential rise fit of the form $(1 - e^{-t/\tau})$ for the 1 to 2.9 eV signal.

The rise time of the 1 to 2.9 eV band was additionally fitted (Figure 3.3) with a rising exponential function of the form:

$$(1 - e^{-t/\tau})$$

Only datapoints between 0.25 ps and 1 ps were considered. This resulted in an estimation for the rise time of (300 $\pm$ 40) fs. The legitimacy of this fit is highly questionable because many datapoints were left out and the starting point of the rise was fixed to $\Delta t = 0$ ps. Additionally, it is not certain that the simple exponential rise model even applies to the physical situation. The fit parameter τ thus only provides a very rough estimate for the rise time.

Table 3.1: Characteristic decay times of the PE signals in Figure 3.4a

Interval / eV	τ / ps	$\Delta\tau$ / ps	t_0
0.2 - 1	1.5	0.1	0.5
1 - 2.9	4.5	0.3	0.8
2.9 - 4	1.2	0.2	0.6
4 - 6	2.0	0.3	0.7

Table 3.2: Two level decay fit parameters of the PE signals in Figure 3.4b

Interval / eV	τ / ps	$\Delta\tau$ \ps	σ / ps	$\Delta\sigma$ / ps	t_0 / ps	Δt_0 / ps
0.2 - 1	1.2	0.2	0.13	0.02	0.50	0.02
1 - 2.9	4	1	0.05	0.01	0.52	0.01
2.9 - 4	1.9	0.3	0.14	0.02	0.65	0.02

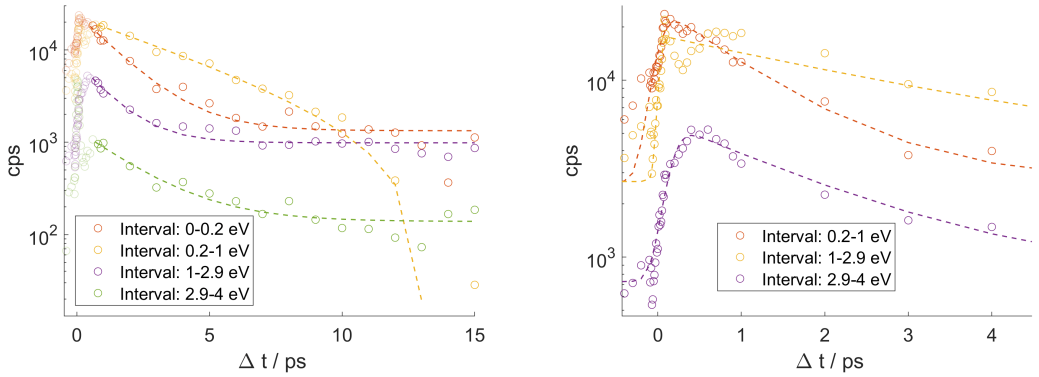

Figure 3.4: Fit results for the PE timescan at high Mg doping conditions (see Figure 3.1), the interval from 4 to 6 eV was not fitted because of a strong crosscorrelation feature. (a) PE signals fitted with exponential decay (b) PE signals fitted with the population function from equation (2.12), closeup near zero time delay.

Term Diagram

The processes which could be the cause of the three signatures (1), (2) and (3) depicted in Figures 3.1 and 3.2 are shown in the energy level diagram in Figure 3.5. The expected energies of possible three-photon processes (2) and (3) are also marked in the PE timescans by white, dashed lines. The white lines (corresponding to a simple estimation of where PE spectrum peaks should appear) are 0.22 eV and 0.26 eV below the maxima of the bands (2) and (3), which is probably caused by interaction of the Mg with the helium environment. The energy difference could also come from an incorrect calibration of the ToF spectrometer at these high energies.
The term diagram (Figure 3.5) shows two scenarios for the origin of the (1) band. The PE signal could either originate from cluster ionization (where Mg clusters have a lower IP compared to free Mg) or from the collapse of the Mg foam, in combination with ionization out of highly excited Mg states. Presumably, the strong band below 1 eV represents a combination of these two channels. The 1 to 2.5 eV signal with its delayed rise from 0.5 to 1 ps could be related to either the foam collapse or cluster fragmentation. A more detailed analysis of the PE bands is given in the discussion.

Ion Signals

Complementary to the PE timescans, an ion timescan was measured (Figure 3.6). The Mg monomer mass signal has a maximum at 40 fs time delay [which is at a similar delay as band (3) in the PE timescan], whereas the mass signals for the dimer and bigger clusters rise slower

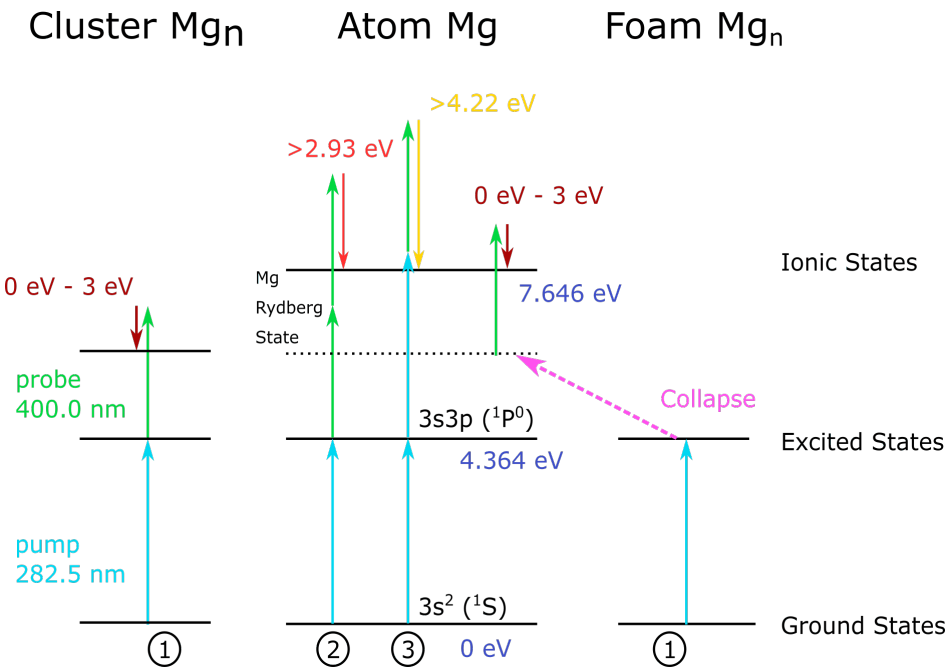

Figure 3.5: Energy level diagram, showing schematically three ionization processes with a pump photon of 282.5 nm (4.39 eV) and a probe photon of 400 nm (3.09 eV) as well as the relevant energy levels of the Mg + He system. The numbers (1), (2) and (3) correspond to the numbers in Figures 3.1 and 3.2. The center shows the energy levels of free Mg, while the left and right levels correspond to Mg clusters and Mg foam respectively. Band (1) could stem from either ionization of Mg clusters or ionization of free Mg out of highly excited states. The energy levels used are listed in Table 2.2.

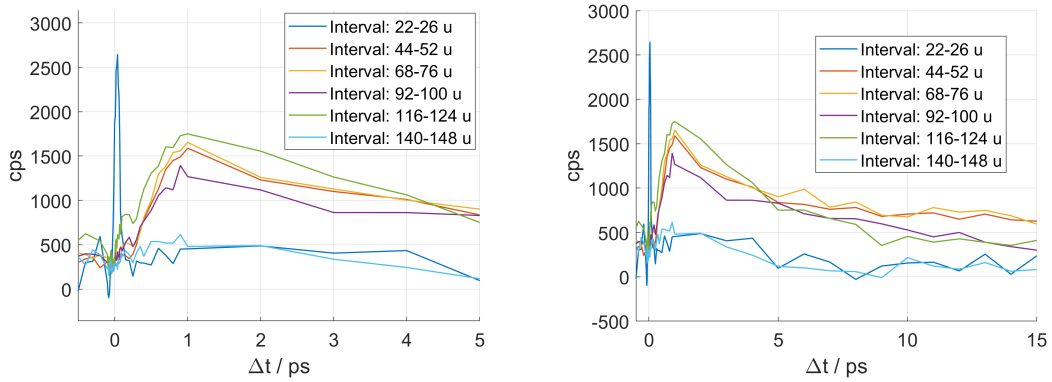

(a) (b)

Figure 3.6: Ion mass integrated signals at high Mg doping conditions, the curves were obtained by integrating within the mass window of $\Delta m = \pm 2$ u centered on the Mg_n masses ($m_{Mg} = 24.3$ u).
(a) Near zero time delay. (b) Entire time delay range. $\lambda_{pump} = 282.6$ nm, $\lambda_{probe} = 401.0$ nm 09.07.20

and are at their maximum at 1 ps time delay. Figures 3.7a and 3.7b show the integrated ion mass signals of $Mg_n + He_N$ (MgHe snowballs). Interestingly, single Mg atoms are almost exclusively detected with He attached. Otherwise, the snowball mass signals increase and decay on similar timescales as the pure Mg_n cluster signals.

Ion Signal Fitting

The mass signals decay with characteristic decay times of 2.5 to 6 ps (fit curves in Figure 3.8a and parameters in Table 3.3). Additionally, the t_0 parameter of the two level fit model is estimated to be about 0.96 ps, which is 0.5 ps larger than the same parameter for the PE signal fits (fit curves in Figure 3.8b and parameters in Table 3.4). This additional delay before the ion signals start to rise is probably due to the time it takes for the excited Mg atoms / clusters to be ejected form the droplet. As discussed in the introduction, when the ionization happens while the excited species is still inside the droplet, no ions are detected.

Table 3.3: Characteristic decay times of the ion signals in Figure 3.8a

Interval / u	τ / ps	$\Delta\tau$ / ps
44 - 52	2.8	0.3
68 - 76	3.0	0.5
92 - 100	6	1
116 - 124	4.0	0.5
140 - 148	2.5	0.7

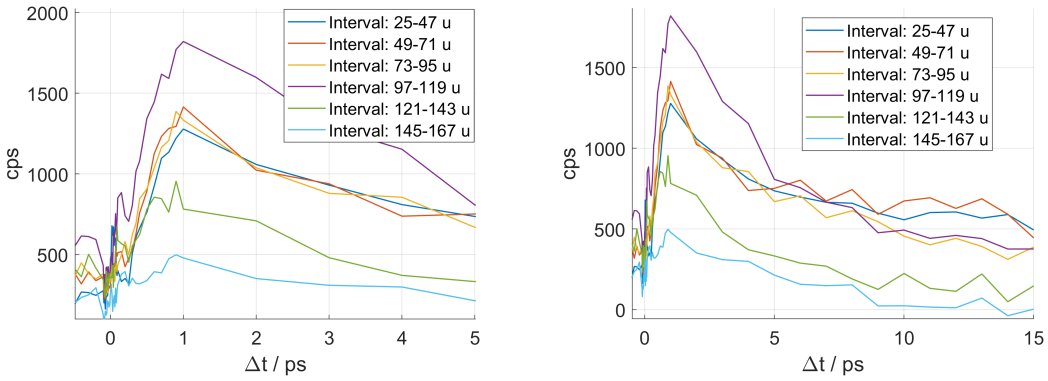

Figure 3.7: Ion mass integrated signals, curves were obtained by integrating between the Mg_n masses ($m_{Mg} = 24.3$ u)
(a) near zero time delay (b) entire time delay range, $\lambda_{pump} = 282.6$ nm, $\lambda_{probe} = 401.0$ nm 09.07.20

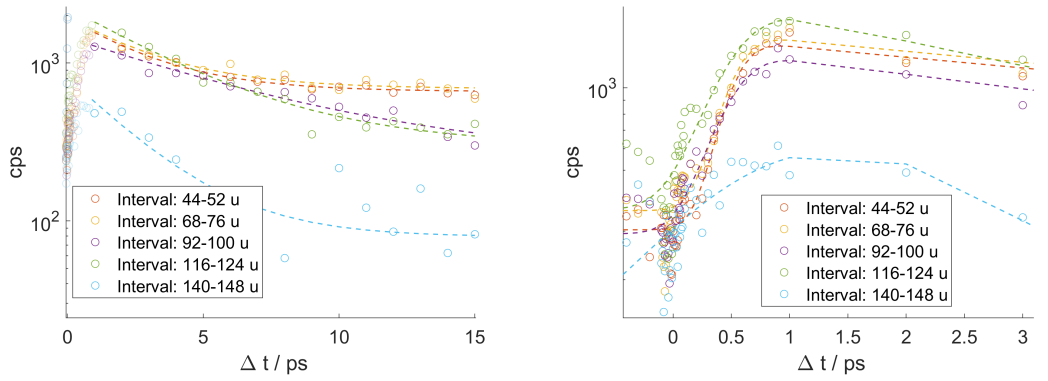

Figure 3.8: Fit results for the ion timescan at high Mg doping conditions (see Figure 3.6), the interval containing the Mg monomer was not included because of a strong crosscorrelation signal. (a) Ion signals fitted with exponential decay. (b) Ion signals fitted with the population function from equation (2.12), closeup near zero time delay.

Table 3.4: Two level decay fit parameters of the ion signals in Figure 3.8b

Interval / u	τ / ps	$\Delta\tau$ \ps	σ / ps	$\Delta\sigma$ / ps	t_0 / ps	Δt_0 / ps
44 - 52	8.4	0.6	0.2	0.02	0.96	0.02
68 - 76	7.8	0.7	0.19	0.03	0.96	0.02
92 - 100	6.0	0.5	0.26	0.03	0.93	0.03
116 - 124	3.5	0.5	0.32	0.04	0.95	0.06
140 - 148	1.1	0.7	0.9	0.2	1	2

Pump Wavelength Scan

In order to gain an understanding for the influence of the pump wavelength on the observed photoelectron dynamics, pump-probe PE spectra at four representative time delays were recorded for three different pump wavelengths. The resulting PE spectra are displayed in Figure 3.9. The 4.7 eV band[2] at 0.02 ps time delay is only present for 282.6 nm, which is at the foam and also near the free Mg resonance. The 3.2 eV band[3] is present for 277.6 nm and 282.6 eV. Most interestingly, the 1 eV band signal increases when the wavelength is decreased, which suggests that this signal does not (or at least not exclusively) originate from the Mg foam, since the wavelength of 272.4 nm (FWHM = 3.6 nm) is not near the foam resonance of 282.5 nm.

The 3.2 eV band also does not shift in energy even though the energy should depend on the pump wavelength (energy of this band consists of $E_{pump} + 2E_{probe} - IP_{Mg}$). No shift in energy is measured because the three photon process only happens when the Mg atom is excited by the pump. This fixes E_{pump} to be close to 282.5 nm, no matter what the pump center wavelength is.

The 3.2 eV band is present for the 277.6 nm pump pulse but not present for the 272.4 nm pump pulse. With a bandwidth of 4 nm (FWHM) the 277 nm pulse is still resonant, where as the 272.4 nm pulse is not.

Probe Pulse Power Scan

The change in amplitude of the PE bands at 3 eV and 4.7 eV was recorded as a function of the probe pulse power. The results can be viewed in Figure 3.10. The spectra are normalized to the low energy band at 1 eV.

The probe pulse power scan showed that band (3) amplitude scales with probe power like the 1 eV band, suggesting that only one probe photon is involved in the ionization process. Band (3) likely originates from a three photon ionization process (two pump photons and one probe photon) as indicated in Figure 3.5. Band (2) scales more strongly with probe power compared to the 1 eV band, suggesting that two probe photons and one pump photon are

[2] 4.7 eV $\approx 2E_{pump} + E_{probe} - IP = (2 \times 4.4 + 3.1 - 7.6)$ eV = 4.3 eV
[3] 3.2 eV $\approx E_{pump} + 2E_{probe} - IP = (4.4 + 2 \times 3.1 - 7.6)$ eV = 3 eV

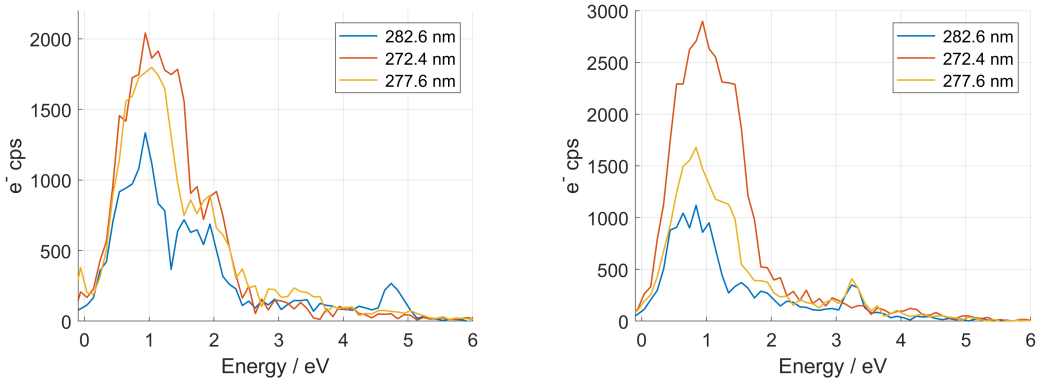

(a) $\Delta t = 0.02$ ps

(b) $\Delta t = 0.2$ ps

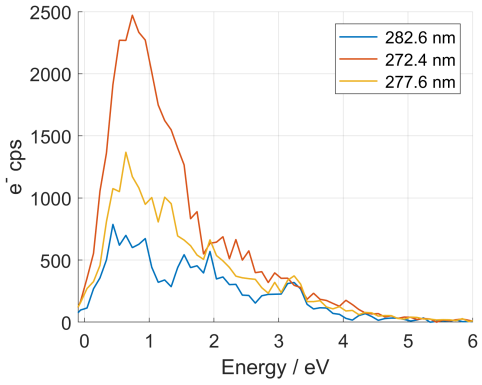

(c) $\Delta t = 0.7$ ps

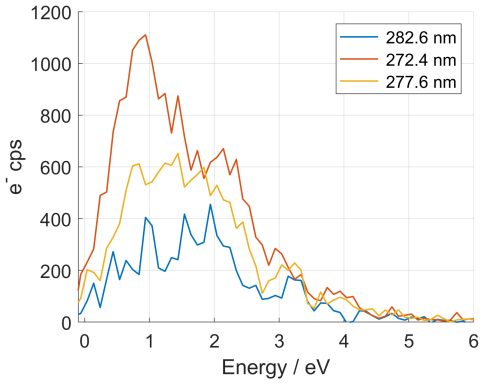

(d) $\Delta t = 2$ ps

Figure 3.9: Pump-probe PE spectra for three different pump wavelengths at representative time delays. 09.07.20

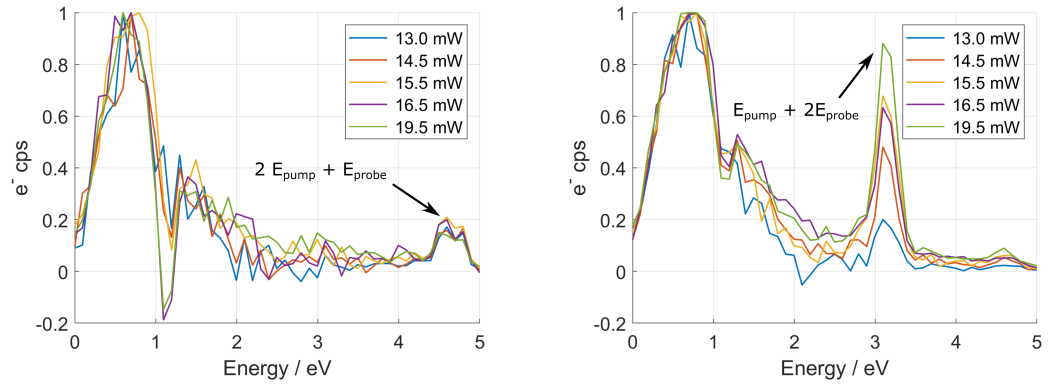

(a) $\Delta t = 30$ fs (b) $\Delta t = 0.2$ ps

Figure 3.10: Comparison of PE spectra at two different time delays and varying probe power, normalized to the <1 eV peak. $\lambda_{pump} = 282.6$ nm, $\lambda_{probe} = 399.6$ nm 08.07.20

involved.

Pump Pulse Power Scan

To rule out unwanted two photon ionization from the pump pulse, which could influence the dynamics, a pump power scan was conducted. Photoelectron spectra at 0.3 ps and 1 ps time delay were recorded for four pump pulse energies (see Figure 3.11). The spectra do not change their shape except for the highest pump power, where a bleach signal appeared at 1 ps and 1.1 eV. The signal strength of the 0 to 2.9 eV signal also scales like the 3 eV peak (visible at 0.3 ps time delay). The similar scaling of the 0 to 2.9 eV band and the 3 eV peak suggests than only one pump photon is involved in the PE energy interval between 0 and 3 eV. This indicates that the dynamics in the 0 to 3 eV energy range are not contaminated by pump pulse ionization.

Pickup Current Dependence of Pump-Probe Spectra

In order to find out how the bands in the PE pump-probe spectra in Figure 3.1 relate to the Mg doping concentration, pump-probe spectra at 0.1, 0.3, 1 and 4 ps time delay were measured in the current range of 26 to 28.8 A. The pickup curves for the particular measurement conditions (Mg pellet refill, new pickup cell) can be found in Figure B.1d.
At each pickup current, the PE spectra were divided into energy intervals. Inside the intervals the counts per second were summed up. This sum for each interval was then normalized to the total counts inside all intervals.
This evaluation results in a plot which shows the relative contribution of each interval to the total electron counts over the pickup current (see Figure 3.12).
Both the 2.9 to 4 eV signal and the 4 to 5 eV signal contribute most to the total counts at

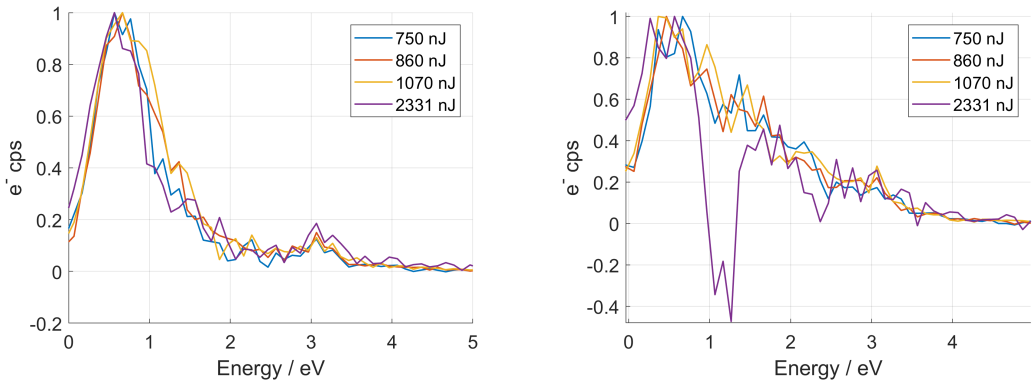

(a) $\Delta t = 0.3$ ps (b) $\Delta t = 1$ ps

Figure 3.11: Comparison of PE spectra at two different time delays and varying pump pulse energy, normalized to the <1 eV peak. $\lambda_{pump} = 398.6$ nm, $\lambda_{probe} = 283.3$ nm 11.09.20

low pickup currents. This is a strong indicator that those signals are related to single Mg atoms inside the droplets.

The 0.2 to 1 eV energy interval is responsible for most counts at high pickup currents. At 4 ps time delay the 1 to 2.9 eV signal decreases for very high pickup currents. This could be explained by the spontaneous collapse of the magnesium foam at high doping conditions.

The 0 to 0.2 eV signal starts to appear for large pickup currents as well, which indicates that it stems from Mg clusters.

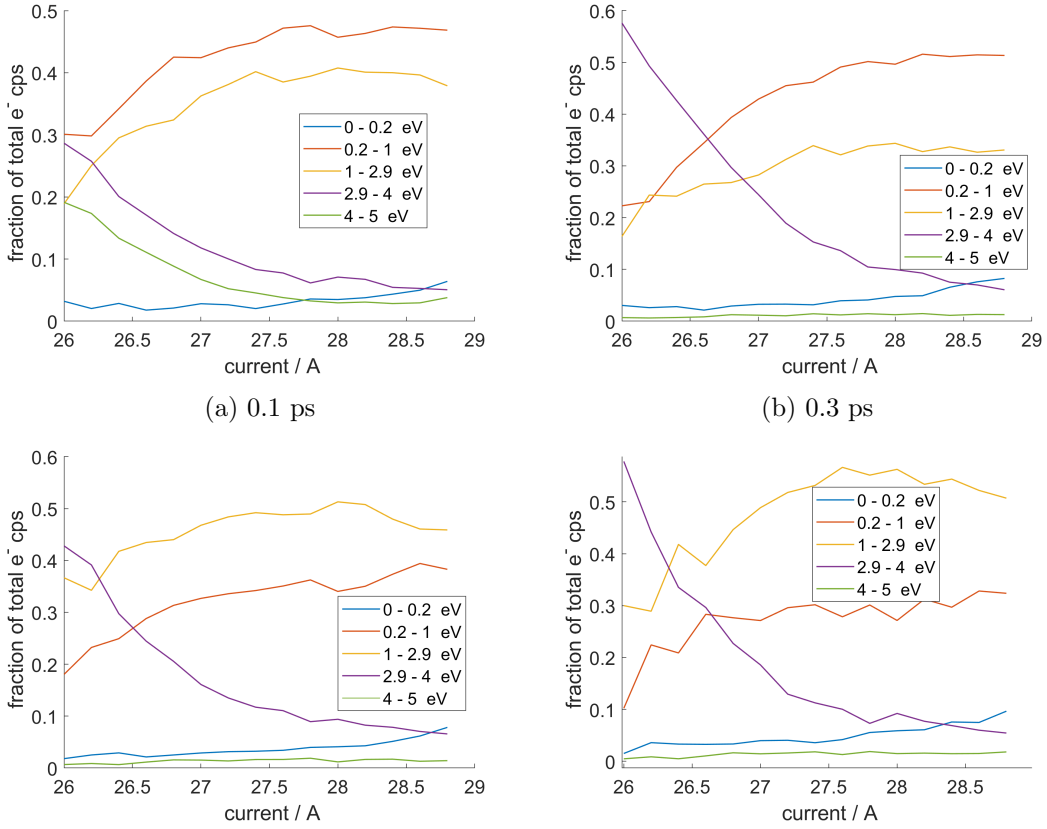

(a) 0.1 ps

(b) 0.3 ps

(c) 1 ps

(d) 4 ps

Figure 3.12: A comparison of fractional counts per second for different PE energy intervals is plotted over the pickup current. The subplots a to d show the curves for four time delays.

3.1.2 281.2 nm pump, 272 nm probe

In contrast to using a 400 nm probe pulse a 272 nm probe pulse allows the detection of electronic states with higher binding energies (up to 4.5 eV). A disadvantage of the higher energy probe pulse is that strong photoelectron signals on both sides of the temporal overlap are visible, because the 272 nm pulse can easily excite magnesium atoms and clusters under investigation if it arrives before the 282 nm pulse. This makes it harder to identify the start of the dynamics near the zero time delay point.

Experimental Parameters

A source pressure of 40 bar and a source temperature of 14 K were used, which gives a mean droplet size of $\overline{N}_{He} = 12500$. The pickup current was about 31 A (see Figure B.1b), which is also in the multiatom pickup regime. The pump pulse center wavelength was 281.2 nm (FWHM 3.5 nm) and the probe pulse center wavelength was 272.0 nm (FWHM 3.5 nm). The photon energies of the pulses were 4.41 eV and 4.56 eV.

Photoelectron Signals

Figure 3.13a shows a PE timescan at positive time delay for a 281.2 nm pump pulse and 272 nm probe pulse. Two bands are visible at 1.4 eV and about 0.5 eV [(1) and (3) in Figure 3.13]. Additionally, the PE spectra around zero time delay show a very broad energy distribution up to about 3.5 eV [see (2) in Figure 3.13c]. The suspected processes behind these bands are shown in the term diagram in Figure 3.14.
The broad feature (2) around zero time delay could come from the transient population of highly excited Mg states caused by the foam collapse.
The 1.4 eV band (1) comes from excitation of Mg to the first excited state ($3s^2 \Rightarrow 3s3p$, see also Table 2.2) and subsequent ionization by the probe pulse. The band exhibits an energy shift to lower energies of 60 meV on a timescale of 350 fs (the energy shift was determined by fitting the maximum of the energy spectrum at each time delay, see Figure 3.13b). The shift is probably due to the bubble expansion. In comparison to the bubble expansion shift of indium the energy shift of magnesium is smaller by about 240 meV. The electron of the indium atom makes a transition to a higher principal quantum number state, whereas for magnesium the excited state has the same principal quantum number. The electron cloud around Mg does not expand as much as around In during excitation, thereby reducing the energy shift caused by the bubble expansion.
The low energy band (3) seems to drift towards 0 eV (see Figure 3.13d). This could be caused by the vibrational relaxation of a hot cluster ground state. The hot ground state could be formed after the foam collapse or from the electronic relaxation of an excited cluster (which was present in the He droplet at zero time delay). The 1.4 eV band (1) seems to appear

only after the broad energy distribution at zero time delay has disappeared, suggesting that a large number of Mg atoms suddenly becomes available for ionization by the probe pulse.

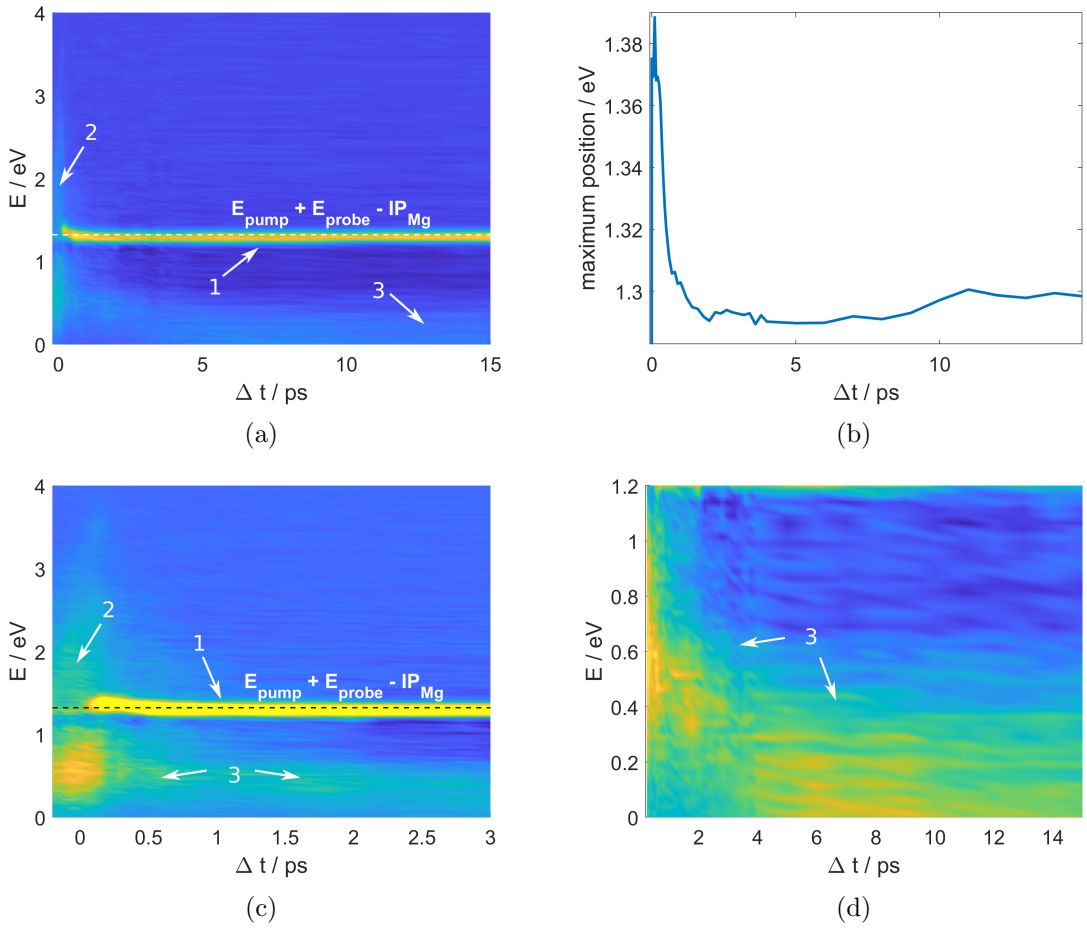

Figure 3.13: (a) PE spectra timescan at high Mg doping conditions (b) Position of the PE spectra maximum obtained by a gaussian fit. (c) closeup near zero time delay, with increased saturation (d) closeup of PE energies between 0 and 1.2 eV. $\lambda_{pump} = 281.2$ nm, $\lambda_{probe} = 272.0$ nm 25.06.20

3.1.3 270.8 nm pump, 281.1 nm probe

Photoelectron Signals

When the roles of the pump and probe pulse are reversed (corresponding to negative time delay side of Figure 3.13) two bands, at 1.1 eV and below 1 eV, are present (see Figure 3.15). The 1.1 eV band corresponds to the ionization of a single Mg atom after excitation ($3s^2 \Rightarrow 3s3p$, see also Table 2.2). The excitation is still possible with the 271 nm pump pulse because it reaches into the Mg absorption band (see Figure 1.4). The energy of this band is lower than in the measurement in Figure 3.13 because the probe pulse of 281.1 nm has lower

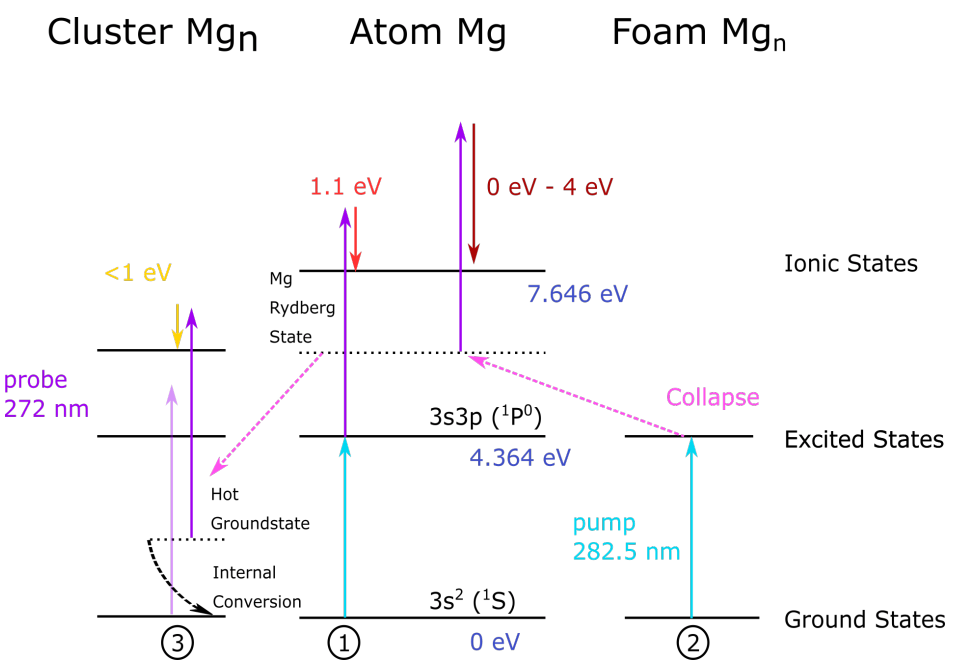

Figure 3.14: Energy level diagram, showing schematically three ionization processes with a pump photon of 282.5 nm (4.39 eV) and a probe photon of 272 nm (4.56 eV) as well as the relevant energy levels of the Mg + He system. The numbers (1), (2) and (3) correspond to the numbers in Figures 3.13. The center shows the energy levels of free Mg, while the left and right levels correspond to Mg clusters and Mg foam respectively. The energy levels used are listed in Table 2.2.

energy than the 272 nm probe pulse.

A discrepancy occurs when calulating the expected PE energies. The energy $E_{pump} + E_{probe} - IP_{Mg}$ is higher than $E_{probe} - (IP_{Mg} - ES_{Mg})$. The problem is that the first method of calculating the PE energy implicitly assumes that the pump pulse center wavelength is exactly resonant with the $3s^2 \Rightarrow 3s3p$ transition. This is not the case for the 271 nm pump pulse. The resonance lies about 0.186 eV lower than the center wavelength, which is the energy difference between the two calculation methods.

The 1.1 eV band does not exhibit an energy shift. It is unclear so far why this happens.

The band below 1 eV is much more pronounced than the low energy band in Figure 3.13. After about 10 ps the low energy band seems to drift out of the ionization window. The broad PE energy feature near zero time delay seen in Figure 3.13 (positive time delay side) seems not present or is overshadowed by the strong low energy band.

The larger signal amplitude of the 0 to 0.5 ps signal suggests that the probe pulse with 281 nm can more easily ionize the species (which is responsible for the low energy signal) than the 272 nm probe pulse. It could also mean that more of the species which is responsible for the low energy band (probably excited clusters) are generated, when the 271 nm pulse is the leading pulse.

The low energy bands in Figures 3.13 and 3.15 could originate from the relaxation of electronically excited clusters followed by vibrational relaxation to the ground state. The bands could also stem from the same species, since both measurements were conducted at similar pickup conditions, and the difference between the maxima of the single Mg band and the low energy band at 2 ps is about 0.85 eV in both measurements.

Ion Signals

For comparison to the PE timescan, Figure 3.16 shows ion mass timescans at negative time delays. Masses 120 u and 144 u can be seen to exponentially decrease while masses below 120 u show a delayed increase and a maximum after 3 ps. This indicates a fragmentation of the larger clusters (120 u and 144 u) into smaller clusters. The integrated signal of the low energy band also has its maximum at 2 to 3 ps. This suggests that the low energy band in Figure 3.15 and the mass signals below 120 u are correlated. However, because the band drifts out of the ionization window, making definitive statements about the ion dynamics is difficult.

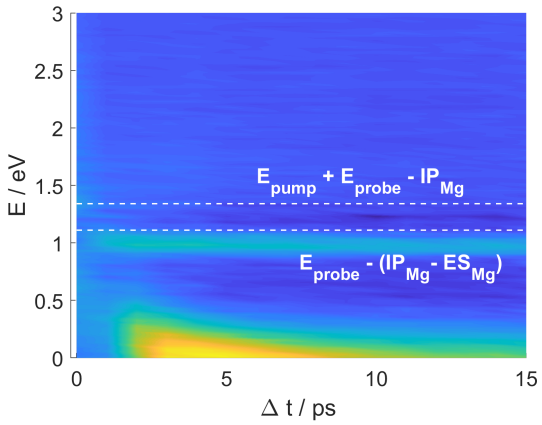

Figure 3.15: PE spectra timescan at high Mg doping conditions, bands at about 1.1 eV and between 0 eV and 1 eV are visible. The energies ES_{Mg} and IP_{Mg} are given in Table 2.2. $\lambda_{pump} = 271.0$ nm, $\lambda_{probe} = 281.1$ nm 26.06.20

3.1.4 PE and Ion Spectra at Symmetric Time Delays

In addition to the timescans shown in Figures 3.13, 3.15 and 3.16 photoelectron and ion spectra were recorded at time delays symmetric around zero time delay. Figure 3.17 shows the measured PE spectra. On both the positive and the negative time delay side a PE energy band corresponding to the ionization of excited Mg atoms from the $3s3p$ state (1.4 eV and

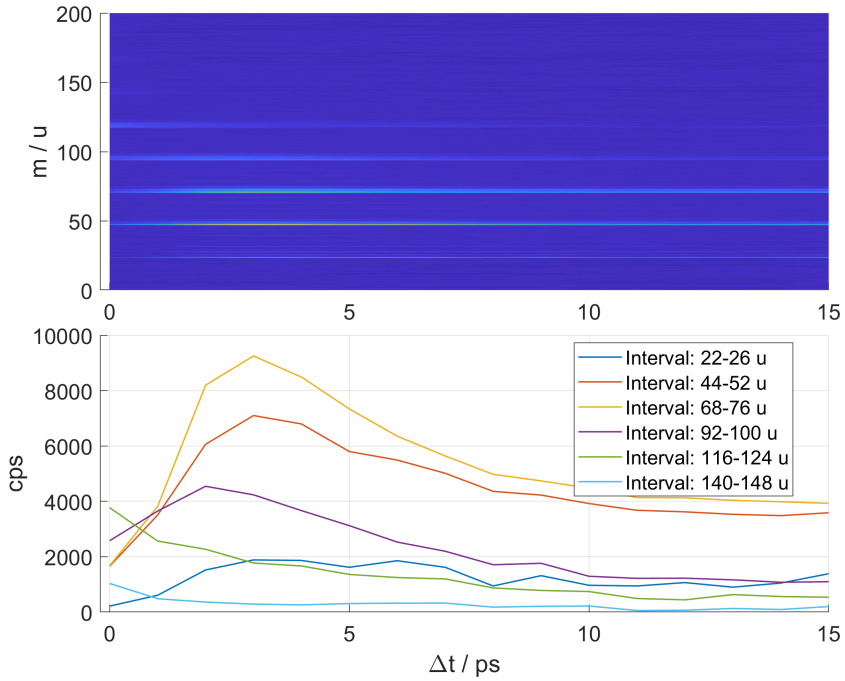

Figure 3.16: Ion timescan at high Mg doping conditions, masses below 120 u show a delayed rise, while 120 u and 144 u show a decay starting from zero time delay. $\lambda_{pump} = 272.0$ nm, $\lambda_{probe} = 281.2$ nm 25.06.20

1.1 eV), a PE band between 0 and 1 eV as well as a broad PE signature around zero time delay are visible. The spectra are similar to the timescans in Figures 3.13 and 3.15. The low energy PE band is more prominent on the negative time delay side (negative time delay meaning 271 nm pump / 281 nm probe). Comparing the peak locations in Figure 3.17 one can observe that the atomic Mg peak is at 1.4 eV when probed with 271 nm and at 1.1 eV when probed with 281 nm. A similar energy shift also occurs for the low energy band which drifts out of the ionization window.

Figures 3.18 and 3.19 show the ion mass spectra as well as integrated mass signals over time delay. On the negative time delay side (Figure 3.19) the integrated mass curves show the same dynamics as in Figure 3.16, that is to say, masses smaller than 120 u show a delayed rise and masses 120 u and 144 u show an exponential decay starting from zero time delay. The ion signal maxima of the integrated signals in Figure 3.19 occur later as compared to 3.16, but this is probably due to only few datapoints in this range.
The integrated ion signal on the positive time delay side (Figure 3.18) shows different dynamics. Here, all clusters (m > 24 u) start their decay at zero time delay, or have maxima around 400 fs (120 u and 144 u). Curiously, the integrated mass signals on the positive time delay side do not match the integrated mass signals for the 400 nm probe pulse experiment

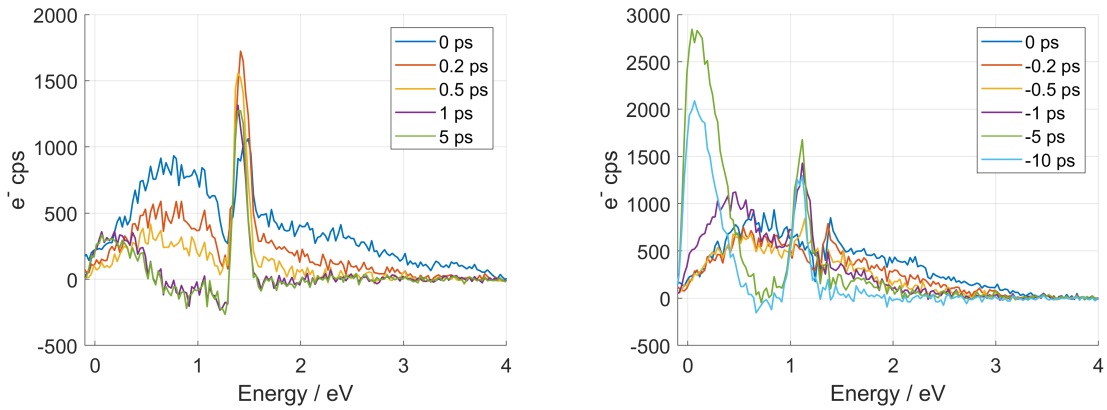

(a) (b)

Figure 3.17: PE spectra at symmetric time delays (high Mg doping conditions), (a) positive time delay side (b) negative time delay side. λ_{pump} = 281.2 nm, λ_{probe} = 272.0 nm 25.06.20

(see Figure 3.6b), in that no ion signal maximum at 1 ps is present. This could be due to a more intense crosscorrelation signal in the 272 probe experiment, or different Mg pickup conditions.
The single Mg atom signal has a maximum at about 200 fs. The difference in ion dynamics on the positive and negative time delay sides suggests that the 281 nm pump pulse triggers other dynamics than the 272 nm pump pulse.

The detection of ions at zero time delay (see Figure 3.16, 3.18 and 3.19) is unexpected. Ionized atoms are trapped within the helium droplets because they usually do not have enough energy to be ejected. The instantaneous detection could be due to almost total evaporation of the helium or due to fragmentation which gives the ions enough kinetic energy for ejection.

3.1.5 282.8 nm pump, 271.3 nm probe

The pump wavelength was increased to closer match the wavelength of the foam resonance (282.5 nm). The resulting timescan (Figure 3.20a) is very similar to the timescan recorded with the 281 nm pump pulse (see Figure 3.13). The broad PE electron feature near zero time delay, the 1.4 eV band and the low energy band between zero and 1 eV are present. The 1.4 eV band shifts by about 0.6 eV towards lower energies.
Increasing the pump wavelength did not make much of a difference in the PE spectra, which is probably due to the bandwidth of the pump pulse already reaching into the foam resonance with the 281 nm center wavelength.

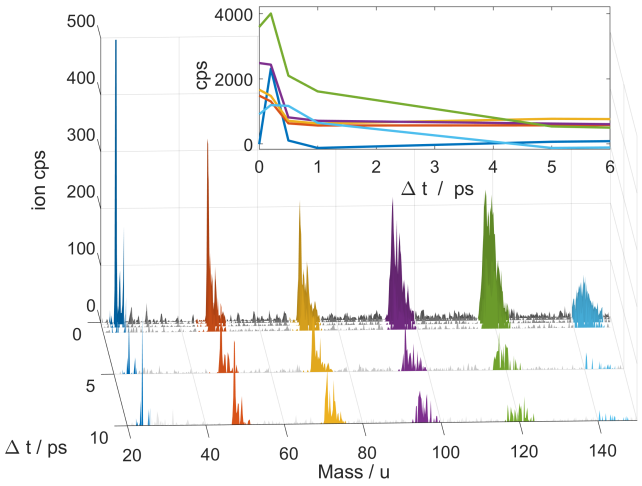

Figure 3.18: Ion mass spectra on the positive time delay side. Inset: Integrated mass signals over time delay. $\lambda_{pump} = 281.2$ nm, $\lambda_{probe} = 272.0$ nm 25.06.20

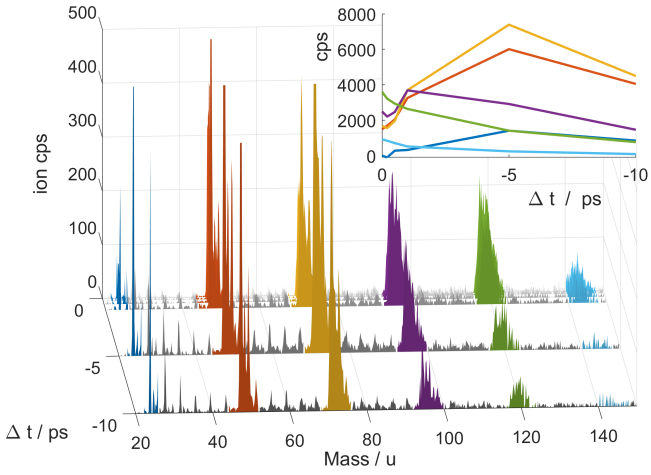

Figure 3.19: Ion mass spectra on the negative time delay. Inset: Integrated mass signals over time delay. $\lambda_{pump} = 281.2$ nm, $\lambda_{probe} = 272.0$ nm 25.06.20

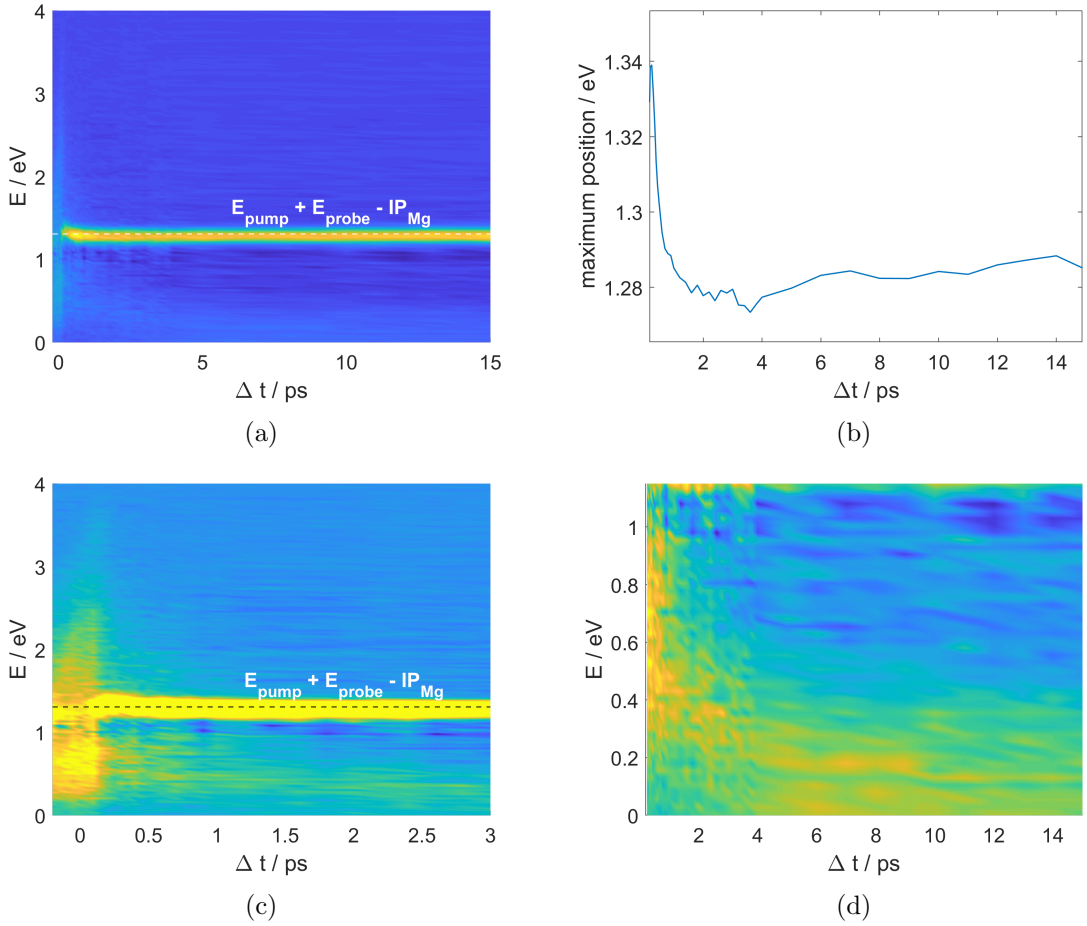

Figure 3.20: (a) PE timescan (b) Position of the PE spectra maximum obtained by a gaussian fit. (c) closeup near zero time delay, with increased saturation (d) closeup of PE energies between 0 and 1.15 eV $\lambda_{pump} = 282.8$ nm, $\lambda_{probe} = 271.3$ nm 26.06.20

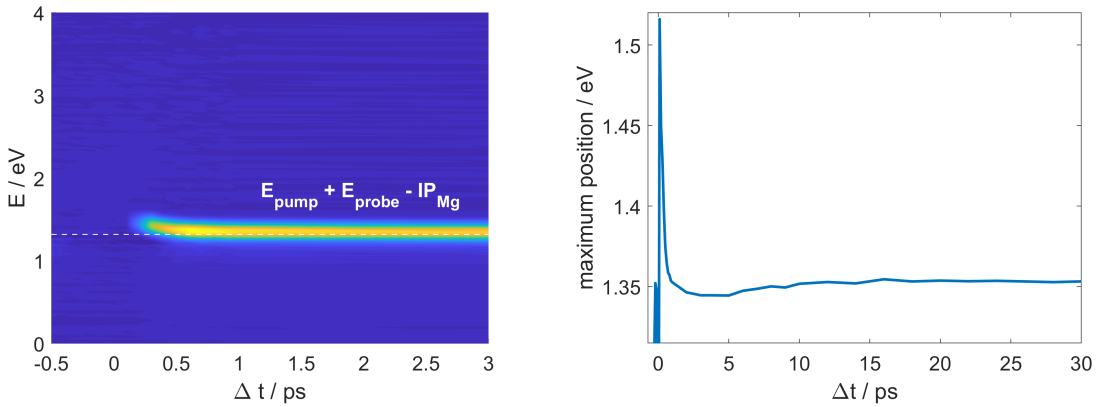

(a) (b)

Figure 3.21: (a) PE timescan at low Mg pickup conditions. (b) Position of the PE spectra maximum obtained by a gaussian fit. λ_{pump} = 281.6 nm, λ_{probe} = 272.0 nm 15.06.20

3.2 Low Doping Concentration

Chronologically the measurements in this section were obtained before the high doping measurements. Only small doping levels were achieved at 30 A because of a less massive Mg source (strips of Mg wire) which was prone to running out during measurements.

Experimental Parameters

The source parameters were 15 K and 40 bar, which correspond to a droplet size of $\overline{N}_{He}$ = 10000. The pickup current was 30 A. The magnesium pickup was not as stable as in the previous sections, and the QMS was not installed at this point.

3.2.1 281.6 nm pump, 272.0 nm probe

Photoelectron Signals

The photon energies for the two pulses were 4.40 eV and 4.46 eV respectively.
For doping conditions with few Mg inside the He droplets, a band at 1.4 eV is visible (Figure 3.21a). The band is caused by ionization of excited Mg atoms $[3s3p\,(^1P^0)]$ inside the droplet. From 0.1 ps to 15 ps the maximum position of the band shifts by −0.17 eV (see Figure 3.21b). The shift is caused by the bubble expansion around the Mg atom. It is twice as large as the energy shift obtained for high doping conditions (see Figure 3.13b). No low PE energy band below 0.5 eV is visible which is different than in high doping condition measurements (see Figure 3.13 and 3.20a). The broad PE energy distribution near zero time delay is also not present (compared to the measurement in Figure 3.13).

3.2.2 266.7 nm pump, 281.8 nm probe

Using a 266 nm pump pulse uncovered new dynamics in the PE and ion spectra. The photon energies of the pulses were 4.65 eV and 4.40 eV. The dynamic presented in this section is likely related to excitation of magnesium dimers at 270 nm (experimentally measured by Lauterwald [13]). Due to he liquid helium environment the 270 nm band likely gets blueshifted so that the 266 nm pump pulse can excite the dimer.

Photoelectron Signals

The PE timescan near zero time delay can be seen in Figure 3.23. At zero time delay two bands at 1.4 eV and 2.4 eV appear, which converge into the Mg single atom ionization band (1.1 eV). The photoelectron signal decays with a characteristic decay time of (19 ± 2) ps (see Figure 3.24).

Potential Energy Curves of the Mg Dimer

In order to find probable causes for the bands in the PE spectra it is useful to look at the potential energy curves of the Mg Dimer (see Figure 3.22). The pump pulse excites the Mg dimer to the $^1\Pi_u$ excited state. From there a wavepacket is launched which can go towards the $^1\Pi_u$ potential energy curve minimum [(3) in Figure 3.22] or dissociate and go towards the Mg + Mg* limit (2). Depending on the time delay between pump and probe pulse the photoelectron kinetic energy changes as the wavepacket moves along the excited state potential energy curve. The ionization can also happen immediately after excitation which is marked as (1) in Figure 3.22. Paths (1) and (2) are also marked in Figure 3.23, because they fit the experimental data reasonably well. There is no band in the PE timescans at 2.1 eV, which suggests that path (3) does not occur. The band at 1.4 eV is not explained by the considered paths. It also cannot stem from the excitation and bubble expansion of single Mg atoms since the pump wavelength (266.7 nm, 3.4 nm FWHM) is too far away from the Mg resonance (285.3 nm). Excitation to higher lying electronic states of Mg is also not possible since the next highest excited state is resonant with 242.7 nm [18]. The origin of the 1.4 eV band near zero time delay thus remains unclear. Apart from the 1.4 eV band, fragmentation of the Mg dimer seems like to most probable explanation for the photoelectron signal.

Ion Signals

The integrated ion signals are shown in Figure 3.25 along with a closeup of the ion signals near zero time delay. The single Mg atom mass rises almost instantly (zero delay is almost in the middle of the rising flank), which indicates that a fragmentation happens which allows the Mg ions to leave the droplet. The fast rise could also be due to cross correlation.
The rising of ion signals of more than one Mg happens at the same timescale as the converging

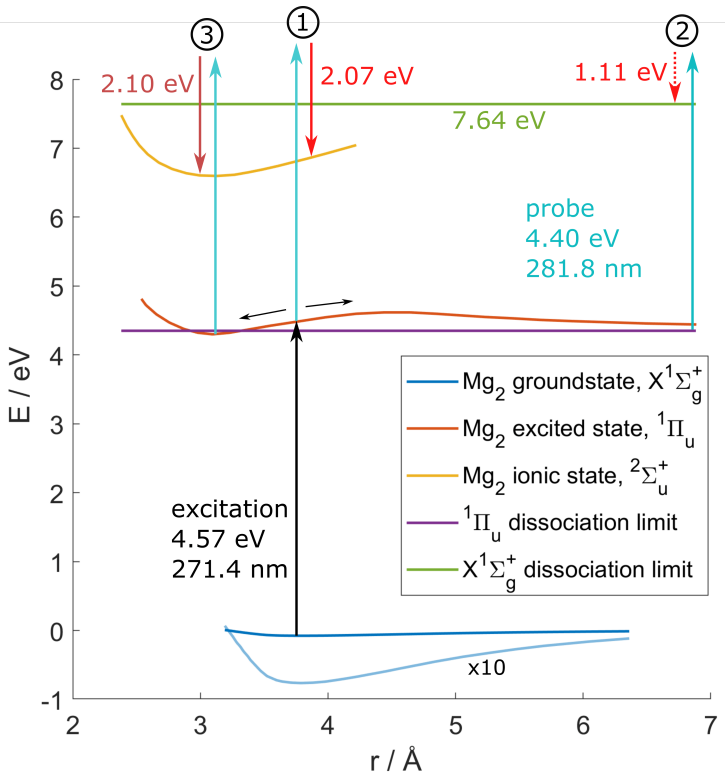

Figure 3.22: Potential Energy Curves of the Mg dimer. Digitized from [23]

of the two bands (2.4 eV and 1.4 eV) into the single Mg band. After the initial fast rise the Mg dimer signal decays with a decay time of (17 ± 2) ps (see Figure 3.25b and Table 3.5). The ion mass signals larger than the dimer mass, which most likely are Mg dimer snowballs, decay on a larger timescale of $\tau = (70 \pm 40)$ ps. The decay time of the Mg dimer signal fits the decay time of the PE band at 1.1 eV. Most of the ion signal comes from the Mg dimer, which does not fit the previous assumption that fragmentation is responsible for the observed data, since a fragmentation would cause a decrease in dimer signal.
In the future a reproduction of this measurement with more control over Mg doping will be necessary to find out where the high energy photoelectron signals in Figure 3.23 come from. A pump wavelength scan would also be beneficial for finding out where the observed photoelectron bands come from.

Table 3.5: Characteristic decay times of the ion signals in Figure 3.25a

Interval / u	τ / ps	$\Delta\tau$ / ps
44 - 52	17	2
52- 150	70	40

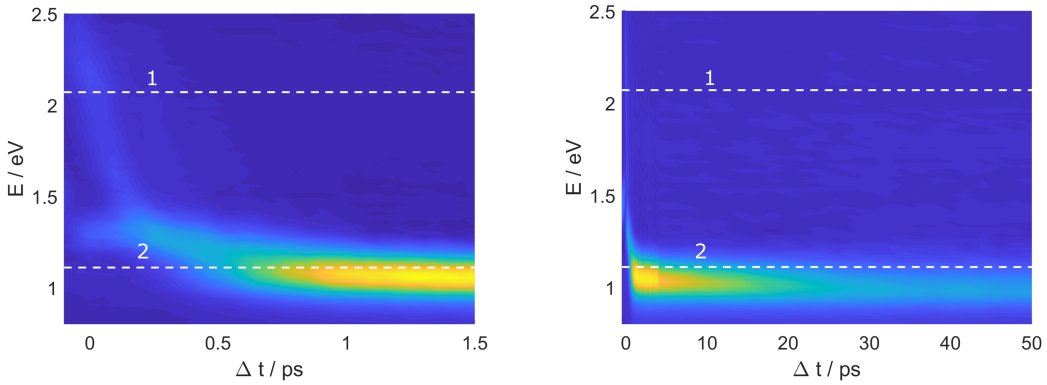

Figure 3.23: (a) PE timescan (b) PE spectra at longer time delay (c) closeup near zero time delay. Numbers 1 and 2 are described in the term diagram in Figure 3.22. $\lambda_{pump} = 266.7$ nm, $\lambda_{probe} = 281.8$ nm 12.06.20

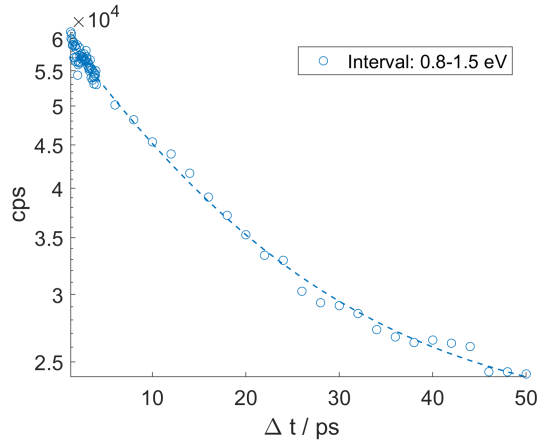

Figure 3.24: Integrated PE signal decay with timeconstant $\tau = (19 \pm 2)$ ps. $\lambda_{pump} = 266.7$ nm, $\lambda_{probe} = 281.8$ nm 12.06.20

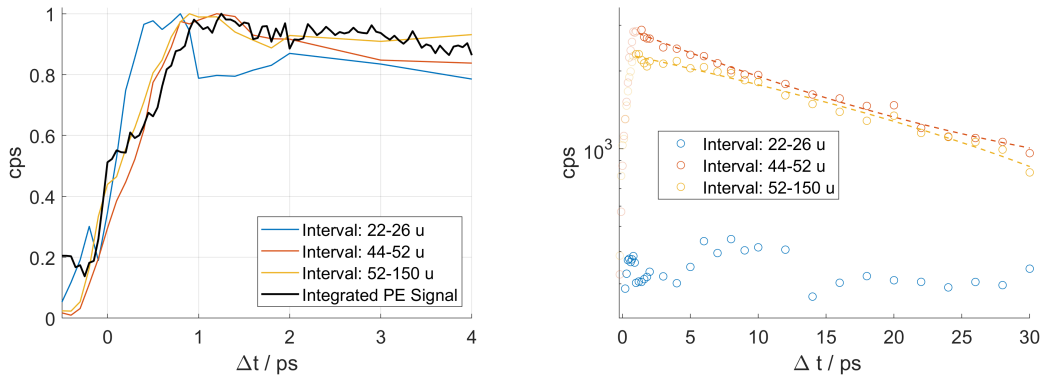

(a) (b)

Figure 3.25: (a) Integrated signals of ion timescan near zero time delay plotted with the integrated PE signal from Figure 3.23. (b) Exponential fit of the ion mass signals. $\lambda_{pump} = 266.7$ nm, $\lambda_{probe} = 281.8$ nm 12.06.20

Chapter 4

Discussion

4.1 Photoexcitation Dynamics of Mg in Helium Nanodroplets

The main goal of this thesis was to find some experimental indicators that magnesium foam (as predicted by the Rostock group [20] [4] [9]) forms in the helium nanodroplets. During the ultrafast collapse of this foam structure energy is released which populates highly excited states of atomic magnesium. With this in mind, an attempt can be made to explain the measured results obtained by time resolved photoelectron and photoion spectroscopy. In order to gain a better understanding for the photoinduced dynamics of magnesium in helium nanodroplets, different scenarios (see Table 4.1) are discussed in this section. A scenario should be able to explain the photoelectron transients as well as the ion dynamics that were measured. The measured data stems from a combination of multiple scenarios.

Table 4.1: Overview of photoexcitation dynamics of Mg_n in He_N

Initial Condition	**Scenario**	**Fragmentation**
clusters present in droplets	1a	-by pump pulse excitation
	1b	-by probe pulse ionization
cluster formed by foam collapse after photoexcitation	2a	-spontaneous, because cluster is hot
	2b	-by probe pulse ionization

4.1.1 Mg Clusters Present before Photoexcitation

Since Mg clusters can form by spontaneous collapse of the Mg foam when the pickup conditions are high enough, we have to consider how the preformed / compact clusters behave after photoexcitation and ionization. Figure 4.1 shows two different scenarios that could occur when a compact Mg cluster is present before photoexcitation. The cluster size is determined by the pickup conditions. One helium droplet most likely contains only one cluster, however different helium droplets can contain clusters of different sizes. The pump pulse excites the cluster and starts off the dynamics.

Scenario 1a: Compact Cluster Present in Droplet, Fragmentation in Excited State

The excitation of the cluster by the pump pulse might lead to fragmentation (see 1a in Figure 4.1). Depending on the arrival time of the probe pulse the fragments are ionized either inside or outside the droplet. Ionization inside the droplet usually cannot be detected, since the ions are strongly attracted to the helium and are not ejected from the droplet. However, depending on the kinetic energy transferred to the fragment, the fragment might be able to leave the droplet even if it is ionized inside. When the fragments are ejected from the droplet they may take helium with them, forming snowballs. All these possibilities have to be kept in mind when discussing ion dynamics and make the measured ion transients very hard to interpret.
Independent of the ejection dynamics the fragments relax out of the ionization window by electronic relaxation and possibly by evaporation of He atoms. The size of the ionization window, and thus the lowest electronic state which can be detected, is given by the ionization potential of the fragment and the probe wavelength.
The delayed rise of the ion signal (see Figure 3.6b) can be explained by the ejection time of the cluster fragments (under the assumption that the kinetic energy is sufficient for ejection). Different fragments might have different ejection times. However, during the fragmentation the fragments can gain a wide variety of velocities, which would smear out ejection time difference for different fragment sizes.
The ion signal decay is similar for all clusters in the recorded data (see Figure 3.6a). One would expect different relaxation times for different cluster sizes. Bigger clusters might have a more metallic character (high density of states), leading to very fast electronic relaxation, while smaller clusters might have more of a van-der-Waals like character (lower density of states), leading to slower relaxation.
The instantaneous rise in the photoelectron signals in the 0 to 1 eV band (see Figure 3.1) could stem from this scenario since the clusters can be ionized immediately by the probe pulse. The photoelectron signal decay can be attributed to the relaxation of the clusters out of the ionization window. However, the delayed rise of the 1 to 3 eV band signal is not explained by scenario 1a, since the probe pulse should be able to ionize the excited cluster immediately after photoexcitation.

Scenario 1b: Compact Cluster Present in Droplet, Fragmentation in Ionic State

This scenario is similar to scenario 1a, except that the cluster does not fragment in the excited state. Instead, the excited compact cluster may be ejected from the droplet (see 1b in Figure 4.1). Ionization then leads to the fragmentation of the cluster. When the cluster is ionized

inside the droplet and its fragments do not have enough kinetic energy for ejection from the droplet, the ionized fragments cannot be detected.
The measured ion signal could be explained by this scenario, since the ion signal rise would be the same for all fragments. The rise time of all fragments is the same as the ejection time for the compact excited cluster. The decay would also be the same for all fragments since it is related to the electronic relaxation of a single excited cluster.
The photoelectron signal for scenario 1b is expected show the same transient behavior as in scenario 1a.

Summary Scenarios 1a and 1b

The expected photoelectron and ion signals for scenarios 1a and 1b are very similar. It is not possible to distinguish between them. However, scenario 1b (fragmentation in the ionic state) seems more likely since the absorption of two photons could more easily lead to fragmentation.

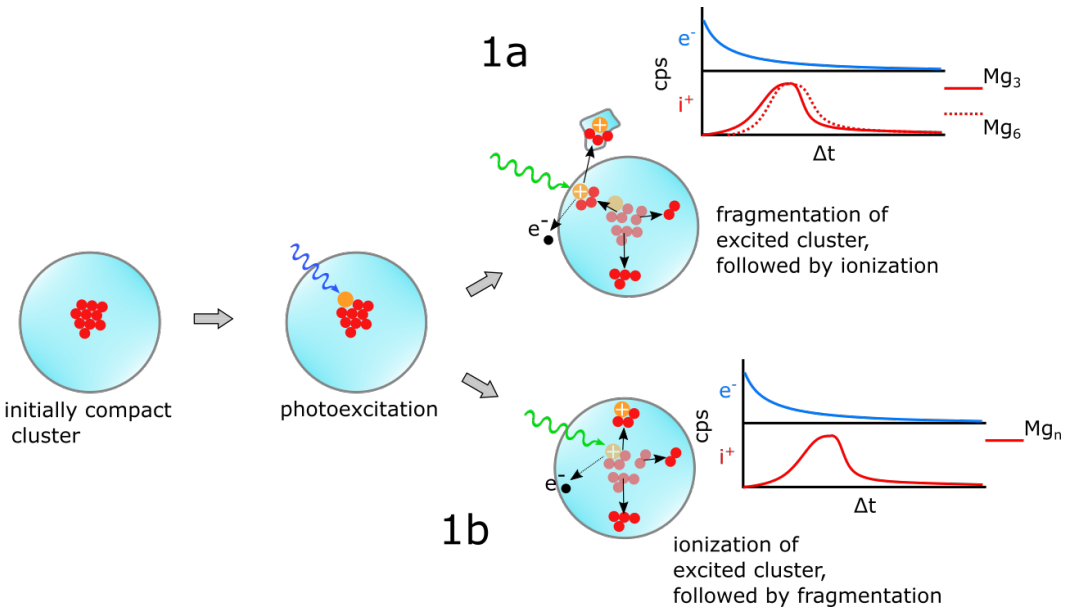

Figure 4.1: Photoionization pathway for initially compact cluster (scenarios 1a and 1b). The insets show schematically the expected electron and ion yields over timedelay for each path.

4.1.2 Mg Clusters Formed by Foam Collapse

When the metastable foam is present inside the helium droplet, the pump pulse triggers the collapse of the foam. This collapse releases energy (on the order of 1 eV per Mg atom [9]) which is transferred to the electrons of the Mg atoms (highly excited states) and to the kinetic

energy of the Mg nuclei. After the collapse a hot metal cluster (meaning the cluster atoms have a lot of vibrational energy) is present inside the droplet.

Scenario 2a: Fragmentation of Neutral Hot Cluster

After the collapse the hot cluster fragments into smaller clusters (see 2a in Figure 4.2). The smaller fragments can be in excited states or in the electronic ground state, and are ejected from the droplet, if their kinetic energy is large enough. The ejected fragments can be detected as snowballs or bare Mg clusters. The fragments can relax electronically by giving off energy to the helium environment or by internal conversion. After some time it is not possible to ionize the fragments anymore because they have left the ionization window.
The delayed ion signal rise could originate from the delayed formation of cluster fragments by the foam collapse, followed by fragmentation. The fragments are then ejected from the droplet. Due to the large distribution of velocities which are possible for each fragment similar signal rise times are expected for ion signals of different Mg clusters. The ion signal decay times for distinct fragment sizes should be different since fragment size influences electronic relaxation times.
When the probe pulse arrives before the foam has had time to collapse no photoelectrons should be detected. This is due to the low photon energy of the 400 nm probe pulse. The ionization potential of Mg atoms loosely bound in the foam is too large for ionization to occur (free Mg has an IP of 7.65 eV). After the foam has collapsed energy is released which excites electrons to higher lying states. Ionization of the magnesium now becomes possible because the higher excited states have a low binding energy and can be ionized by the 400 nm probe pulse. Excited cluster fragments that form during the foam collapse may also be ionized by the 400 nm probe pulse.
In either case a delayed rise of the photoelectron signal is expected, which fits the behavior of the photoelectron energy band between 1 and 3 eV (see Figure 3.1).

Scenario 2b: Fragmentation of Ionized Hot Cluster

This scenario is similar to scenario 2a except that the fragmentation happens when the hot cluster is already ionized (see 2b in Figure 4.2) and could explain the delayed ion signal rise with similar timeconstants for all fragments (see Figure 3.6a). The ion signal rise times are then determined by the foam collapse time. The similar ion signal decay times are also explained since the decay of all cluster fragment signals is related to the electronic relaxation of the hot cluster out of the ionization window.
For the photoelectron transients a delayed signal rise is expected, similar to scenario 2a.

The fragmentation of the ionized hot cluster formed after the foam collapse is able to explain both the similar rise and decay times of the ion signal for different fragment sizes and

the delayed photoelectron signal rise of the 1 to 3 eV band.

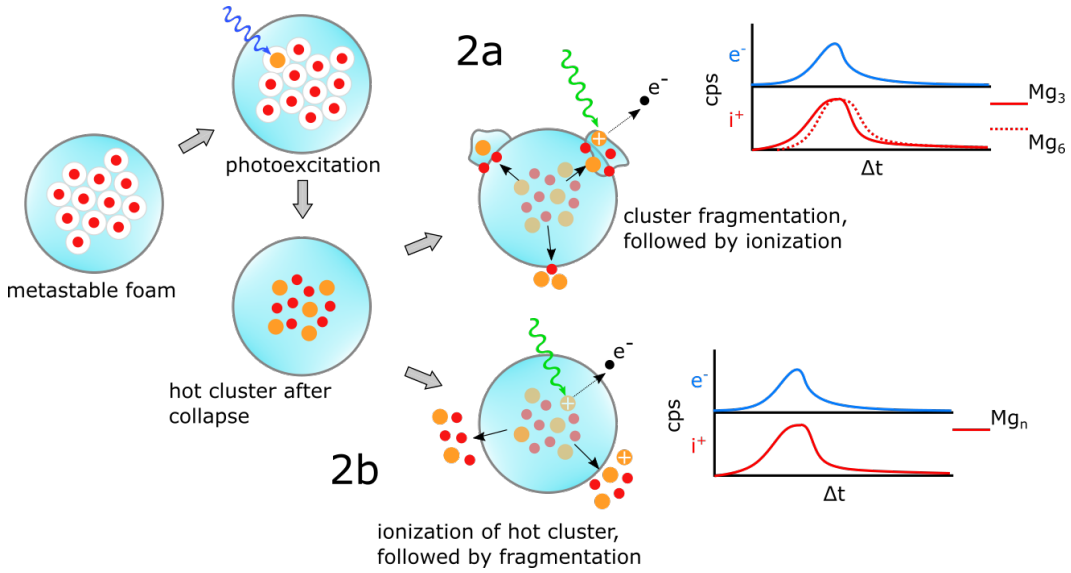

Figure 4.2: Photoionization pathway for the magnesium foam (scenarios 2a and 2b). The insets show schematically the expected electron and ion yields over timedelay for each path.

4.2 Indicators for the Foam Collapse

The delayed signal rise of the 1 to 3 eV photoelectron band, which has an exponential rise constant of (300 ± 40) fs (see Figure 3.3) and a signal maximum of the 1 to 3 eV band at about 800 fs are the strongest indicators for the foam collapse. The 0.2 to 1 eV signal can be assigned to the dynamics of preformed Mg clusters due to its instantaneous rise at zero time delay. It increases at very high Mg doping conditions, whereas the 1 to 3 eV signal decreases (see Figure 3.12). This is expected to happen because the foam inside the droplets collapses spontaneously for high magnesium doping conditions (see Figure 1.7b). The delayed rise of the ion signal could be related to the foam or the cluster scenarios. The similar rise time of the ion signals as the 1 to 3 eV photoelectron band might even indicate that the delayed ion signal rise is related to the foam collapse and fragmentation of the hot cluster. However, because the helium environment strongly influences the ions, no clear distinction can be made using the available experimental data.

Chapter 5

Conclusion

Time resolved photoelectron and photoion spectroscopy was used to study the photoexcitation dynamics of Mg inside helium nanodroplets. By employing a 400 nm probe pulse, a photoelectron signal, corresponding to photoelectron energies of 1 to 2.9 eV (1 to 2 eV binding energy), was found (Figure 3.1). This signal is a strong candidate for a signature from the magnesium foam collapse, as predicted in the literature (see [20] [4] [9]). Assuming this signal really comes from the foam collapse, a collapse time of about (300 ± 40) fs can be assigned using an exponential rise fit (Figure 3.3).
A larger probe ionization window (272 nm) was also used, which enabled the study of the dynamics of more tightly bound states. A fast dynamic is also visible at high photoelectron energies for the 272 nm probe pulse, likely caused by the same phenomenon as the dynamic seen in the 400 nm probe experiments. Additionally a slow relaxation dynamic (timescale of 15 ps) was found for low photoelectron energies (Figure 3.13).
For the photoelectron signal from the Mg 3s3p excited state, a shift in photoelectron energy after 2 ps was observed. The energy shifted by 60 to 80 meV for high doping conditions and 150 meV for single Mg atom pickup (Figures 3.13 and 3.21a). The difference most likely comes from difficulties in fitting the maximum in case of the high Mg doping measurements. The shift can be assign to the bubble expansion of helium around the Mg dopant. This expansion was previously studied in depth for the indium as the dopant atom [27] [26]. For the indium atom the shift in photoelectron energy was about 300 meV after 1 ps. The shift is smaller for magnesium because the principle quantum number of its electronic state does not change during excitation ($3s^2$ to $3s3p$). This leads to a smaller bubble expansion compared to the indium which in turn does not increase the excited state energy of the Mg 3s3p state as much.
For low Mg doping conditions and λ_{pump} = 267 nm / λ_{probe} = 282 nm a very fast dynamic was discovered (Figure 3.23). A photoelectron band is visible which shifts by 1.5 eV after 1 ps. The exact cause of this dynamic is unknown but it might be related to the dynamics of a Mg dimer. The time-dependent ion signals were also measured (Figure 3.25) but no interpretation can be given so far.

5.1 Outlook

In order to extract more information about the magnesium foam collapse out of the transient ion signals, Photoelectron Photoion Coincidence (PEPICO) spectroscopy could be used. This method allows to measure correlations between the photoelectron and ion signals. It was already succesfully applied to the dissociation dynamics of acetone [14] [10]. The Mg doping level dependence of the ion signals could also be measured in order to get a rough insight into which photoelectron signals are associated with which cluster signals.
An excitation wavelength scan toward longer wavelengths than 282.5 nm could also help clarify which photoelectron signals come from the cluster and which come from the foam. The cluster signal seems to increase for excitation wavelengths shorter than 282.5 nm, as seen in the wavelength scan done in this work (Figure 3.9c).
A global fit procedure could be applied to the measured photoelectron timescans in the future to extract decay constants for different parts of the spectra (decay associated spectra). The feasibility of the global fit procedure was demonstrated on the photoexcitation dynamics of acetone [7].
The fast dynamic on the negative time delays side (discussed as the Mg dimer signal in this work) could be very interesting to study further. It could reveal insights into the fragmentation dynamics of diatomic molecules inside of superfluid helium.

Appendix A

Characterization Measurements

A.1 Optimal Laser Focus Height and Nozzle Skimmer Distance

The optimal laser focus height was determined by using a 800 nm laser pulse to ionize indium atoms in helium nanodroplets (source parameters: 40 bar, 15 K. focal length $f = 1\ m$). This was done for three coldhead nozzle to skimmer distances. Since the skimmer tip is very delicate and should not be touched, the distance between the skimmer tip and the nozzle could not be measured directly. Instead, a complementary distance d from the source chamber wall to the back of the skimmer holder was measured for documentation purposes (see Figure A.1). For the smallest distance between nozzle and skimmer tip ($d = 17.5$ mm) no InHe signal

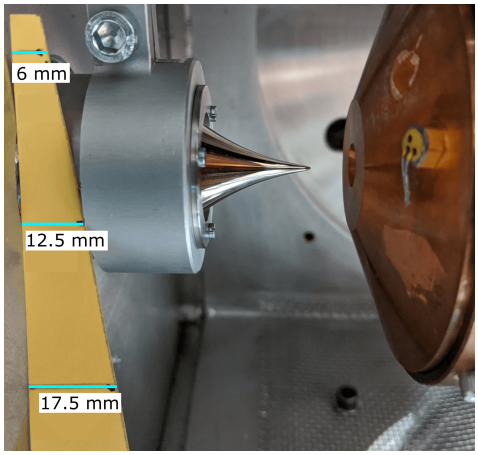

Figure A.1: Nozzle-skimmer distances. The yellow paper strip was used to measure the approximately measure the complementary distance d.

was present, which suggests that no droplets formed. When the skimmer is too close to the nozzle, it could cause the formation of a shockwave structure near its tip. This shockwave then prevents formation of droplets. The results for the intermediate ($d = 12.5$ mm) and large distance ($d = 6$ mm) are displayed in Figure A.2a.
The laser focus height was measured using the repeller z position, the laser beam was always

positioned 3 mm above the top of the repeller. The intermediate nozzle skimmer distance brought a signal increase of about 40% as compared to the large nozzle skimmer distance at the optimal position of repeller position of 13.4 mm.
Figure A.2b shows InHe above threshold ionization (ATI) PE spectra for the three nozzle skimmer distances. At the intermediate distance photoelectrons with higher energies are present, corresponding to larger helium droplets. When the skimmer is close to the nozzle ($d = 6$ mm) almost no ATI signal was measured, which indicates that no droplets were generated. Due to the signal improvement, the intermediate nozzle-skimmer distance was used in this thesis.
A further increase in the helium droplet signal might be possible at $d = 9$ mm or $d = 15$ mm. Changing the skimmer- nozzle distance has two opposing effects: A smaller distance means more of the helium beam can fit through the skimmer opening, increasing the helium signal. However, at some small distance the skimmer tip starts to influence the expansion, thereby preventing droplet formation.

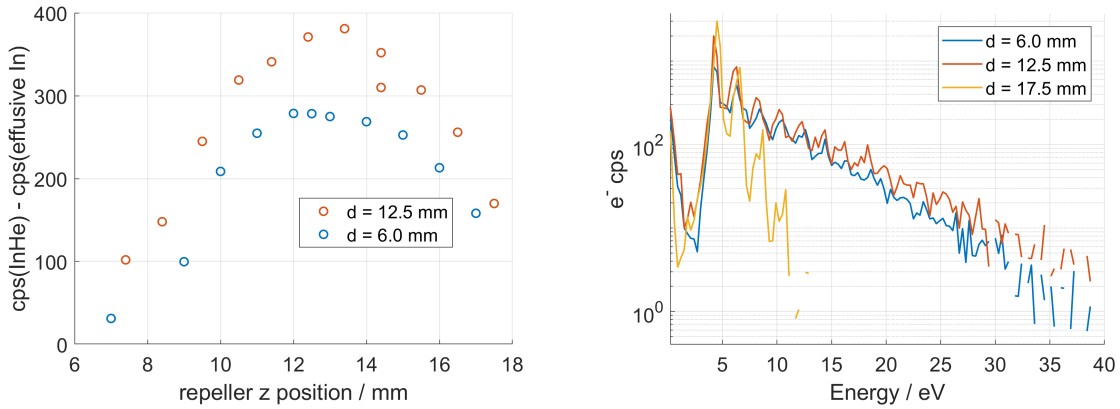

(a) (b)

Figure A.2: InHe PE cps for different repeller z positions (z = laser focus height - 3 mm) and two nozzle to skimmer distances. (b) InHe above threshold ionization PE spectra for three nozzle to skimmer distances. The length d is complementary to the nozzle skimmer distance and it is measured from source chamber wall to the back of the skimmer holder. The eiToF filenumbers for the curves are: 32993 (yellow), 33015 (orange), 32986 (blue).

A.2 Optimal Coldhead Nozzle Position

For the largest nozzle to skimmer distance (complementary distance $d = 6$ mm) the coldhead nozzle position transverse to the helium beam axis was changed (vertical shift z, horizontal shift x) while measuring the amount of single He present in the main chamber using a leak tester connected to the main chamber prevacuum ("leakrate": we want a leak as big as

possible through the skimmer), the pickup chamber pressure p_{PUC} and the main chamber pressure p_{MC}. The origin of the coordinate system (x, z) was chosen to coincide with the maximum leak rate of He in the mainchamber prevacuum. Figure A.3 shows the measured quantities leakrate, p_{MC} and p_{PUC} over nozzle position (x, z). At the origin $(x = 0, z = 0)$ a big spike is visible in Figures A.3a and A.3b which marks the best nozzle position.

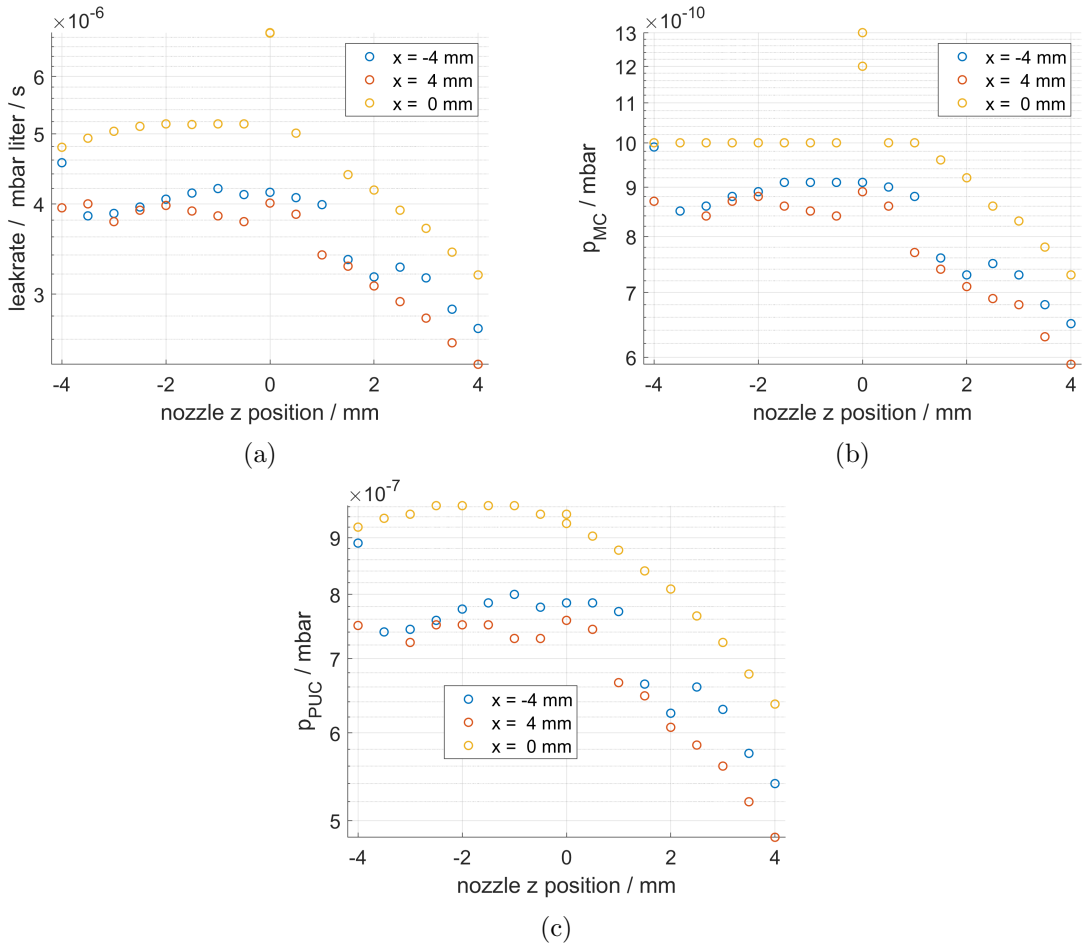

Figure A.3: (a) Leakrate of single He in the mainchamber prevacuum. (b) The main chamber pressure p_{MC} (c) The chamber pressure p_{PUC}. All quantities plotted over nozzle z position and three nozzle x positions. 27.01.20

Appendix B

Magnesium Pickup

B.1 QMS Pickup Curves

The QMS currents for Mg clusters were measured as a function of the oven heating current (see Figure B.1). The pickup curves were used as a tool for choosing the right current for the desired pickup conditions (Mg monomer, dimer or multiatom pickup). The decrease of the 8 u signal as the current is increased is related to the complete evaporation of the helium nanodroplets, when a large number of dopant atoms is picked up. This decrease also influences the other curves. To promote the formation of Mg foam it seemed reasonable to choose a current just above the maximum of the Mg_4 curve.
The location of the curve maxima is dependent on the type of Mg sample used (wire versus pellet) due to the surface area dependence of the vapor pressure as well as the amount of Mg inside the oven. The pickup cell geometry also plays a role. After a refill of the oven it may be necessary to remeasure the pickup curves.

B.2 Current Dependence of PE Spectra

As the pickup current ($\propto$ Mg doping level) is changed a change in the photoelectron spectra can be observed. This is shown for the pump-only and probe-only PE spectra in Figure B.2. For higher Mg doping levels, a very broad structure appears in the pump- and probe-only spectra, which is most likely the result of two photon ionization of Mg clusters.
Photoelectron spectra at four different pickup currents were measured on the positive time delay side. The resulting spectra can be seen in Figure B.3. The broad PE feature at zero time delay and the low energy band appear as the current is increased, while the 1.4 eV band is always present. The features that get more prominent with higher current thus seem to stem from processes which involve multiple Mg atoms. It could be argued that the features do not shift as the current is increased, however the PE spectra are very noisy at 29.5 A and 30 A. PE spectra were also recorded on the negative time delay side (Figure B.4).
The band that appears between 0 and 1 eV at high Mg doping levels in Figures B.3 and B.4 is the same band which appears in in Figures 3.17b and 3.15.

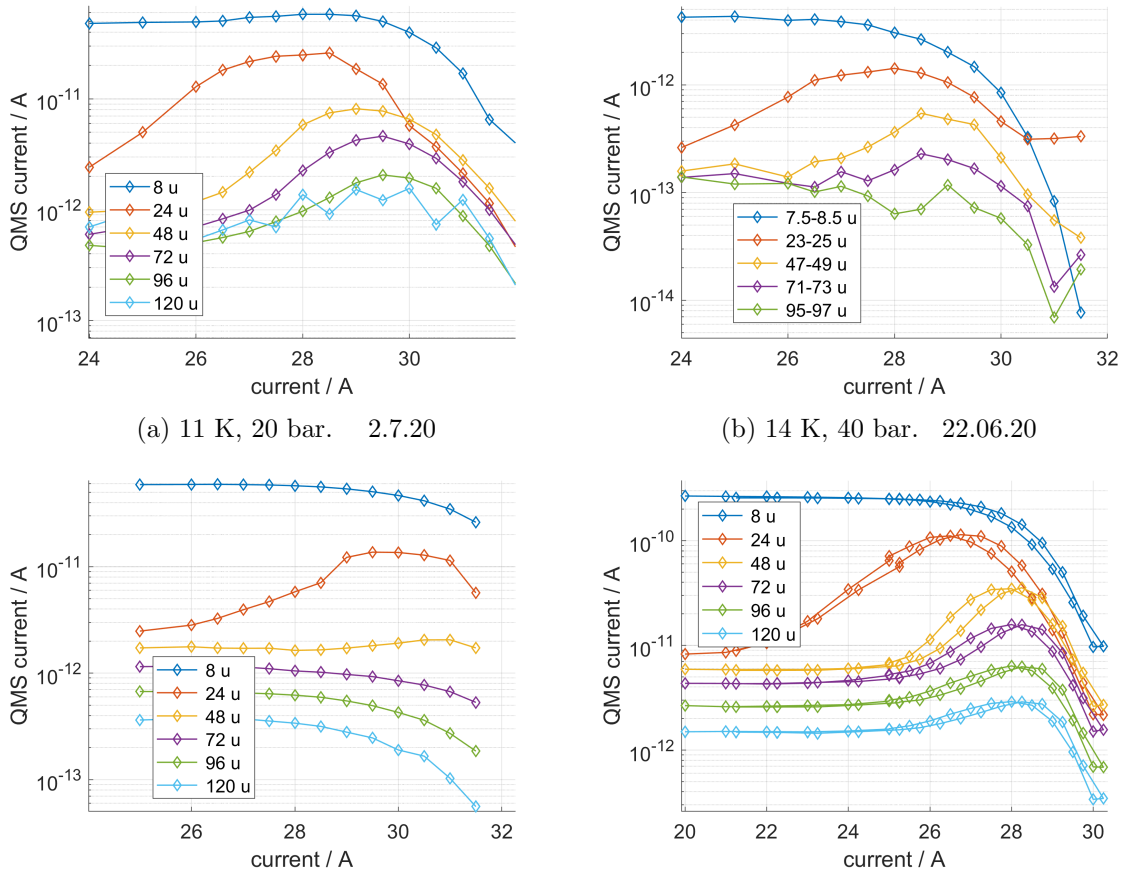

(a) 11 K, 20 bar. 2.7.20

(b) 14 K, 40 bar. 22.06.20

(c) 15 K, 20 bar. 06.07.20

(d) 11.6 K, 20 bar. 08.09.20

Figure B.1: Magnesium pickup curves for different helium droplet source parameters. The curves on the lower right show a hysteresis which is was caused by not giving the system enough time to thermalize after heating up / cooling down.

B.3 He Source Parameter Dependence of PE Spectra

Pump-probe PE spectra were measured at a time delay of 0.2 ps for various helium source parameters (see Table B.1). The spectra are displayed in Figure B.5. The broad photoelectron band from 0 to 4 eV increases relative to the Mg monomer signal as the source temperature is decreased. The signal does not shift as the source temperature is changed.

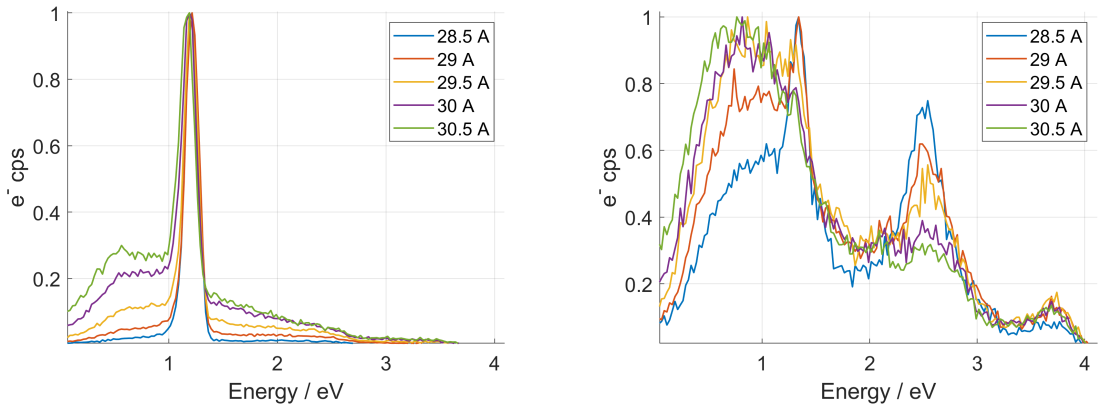

(a) Pump-only PE spectra

(b) Probe-only PE spectra

Figure B.2: Pump-only and probe-only PE spectra for various Mg pickup conditions (normalized to the maximum of the spectra). $\lambda_{pump} = 281.2$ nm, $\lambda_{probe} = 272.0$ nm 25.06.20

Table B.1: Helium source parameters and an estimation for the mean number of helium atoms in the droplet (read off from Figure 2.2c) associated with the pump-probe spectra in Figure B.5. The mean droplet numbers with an asterisk are very rough estimates as there is no data available in Figure 2.2c for pressures other than 40 bar and 20 bar

p_{He} / bar	T / K	$\overline{N}_{\mathrm{He}}$
40	14.0	13000
35	13.0	17000*
30	12.0	18000*
25	11.6	19000*
20	10.9	20000

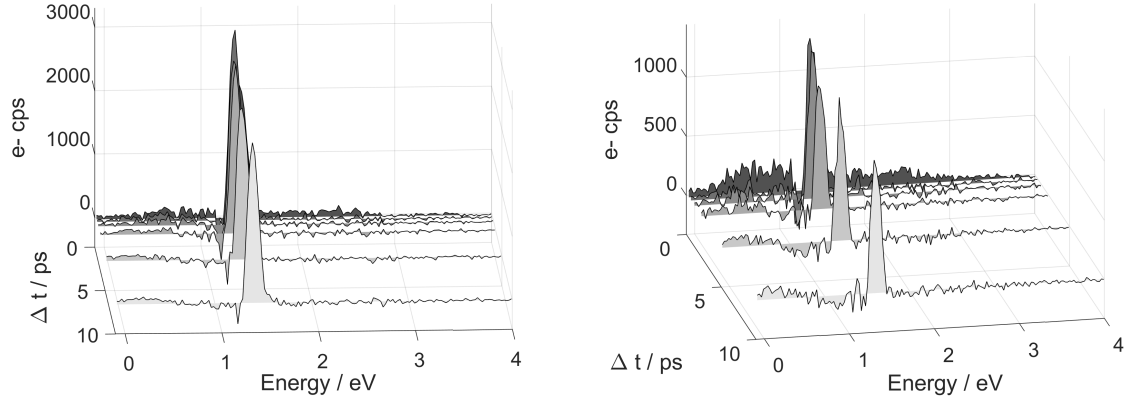

(a) 29 A

(b) 29.5 A

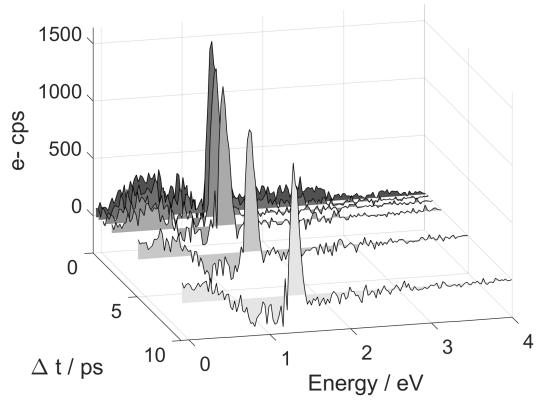

(c) 30 A

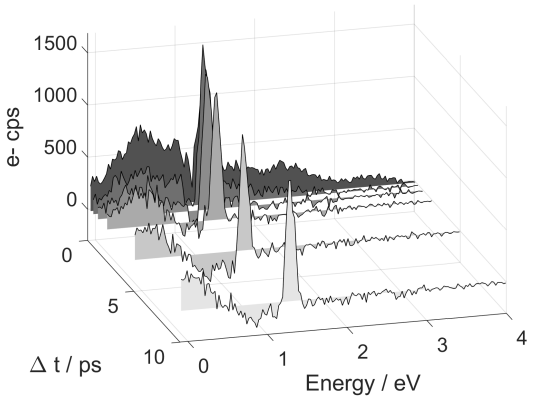

(d) 30.5 A

Figure B.3: Comparison of PE spectra for different pickup currents. $\lambda_{pump} = 281.4$ nm, $\lambda_{probe} = 271.8$ nm 24.06.20

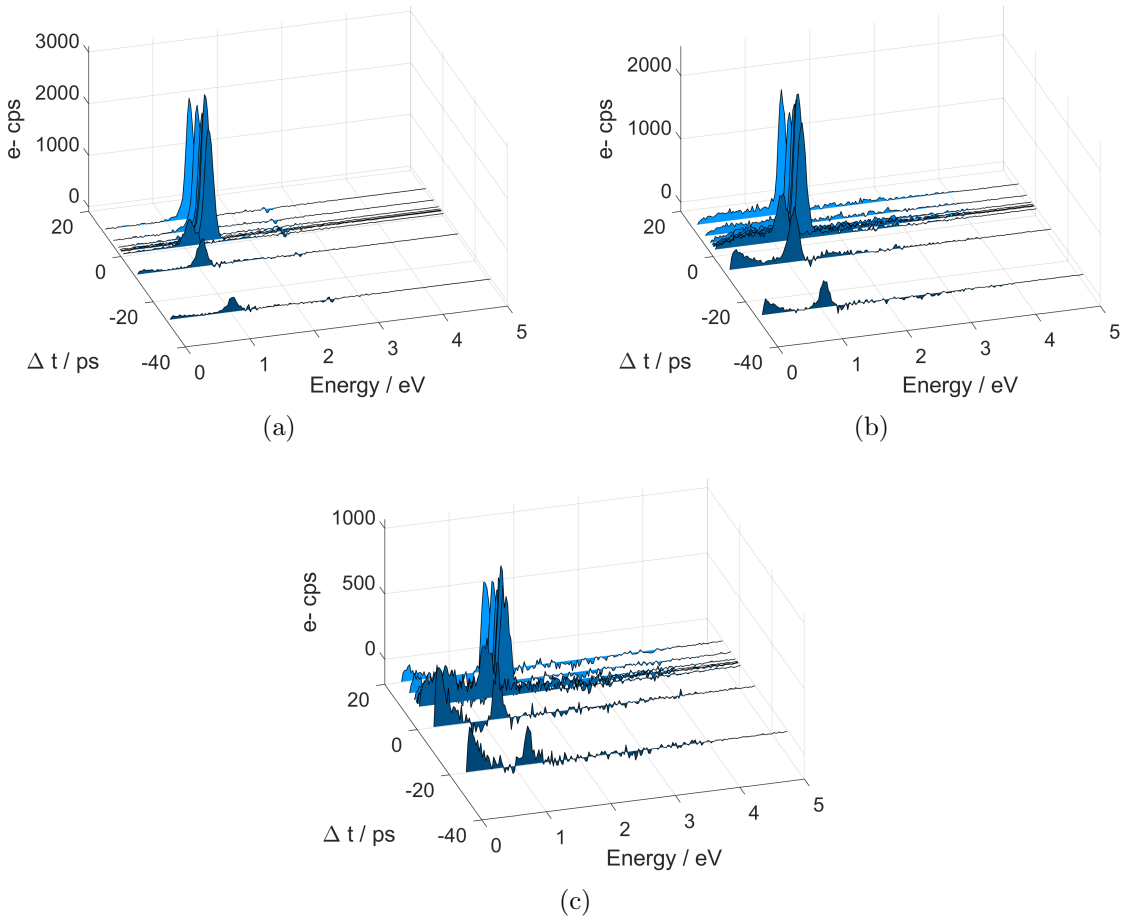

Figure B.4: Comparison of PE spectra for different pickup currents, negative time delay side. $\lambda_{pump} = 281.2$ nm, $\lambda_{probe} = 271.2$ nm 18.06.20

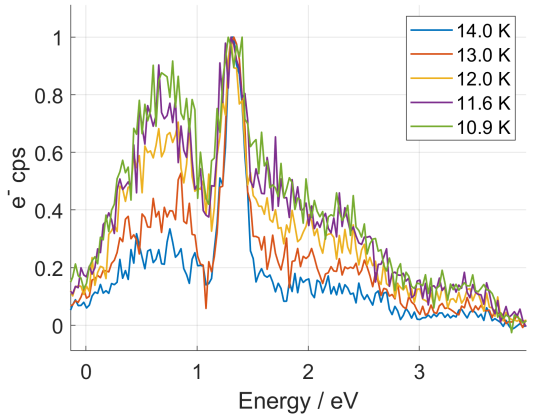

Figure B.5: Normalized pump-probe PE spectra at 0.2 ps time delay for different helium source temperatures ($\propto$ helium droplet size). $\lambda_{pump} = 282.8$ nm, $\lambda_{probe} = 271.3$ nm 26.06.20

Appendix C

Laboratory Devices and Programming

C.1 Magnesium Source

Thin Mg stripes and Mg pellets were used as magnesium sources. A big problem with the Mg stripes was a relatively short lifetime in the resistively heated oven. Sometimes measurements would show instability over time which was caused by the depletion of magnesium. Switching to more massive Mg pellets (Figure C.1) solved this issue.

Figure C.1: Magnesium pellets in the ceramic pot, which is resistively heated inside the pickup chamber.

C.2 Adding the Source Chamber Turbomolecular Pump to Oversight

The source chamber turbomolecular pump was added to the oversight system, which is used to monitor vacuum chamber pressures, the temperature of the helium source and the cooling water pressure. The RS232 service connector is used to read out pump parameters. So far it was not possible to control the pump using this connector. The code listing for the python class which is used by the oversight system is given below.

Listing C.1: Python class which is used to aquire parameters from the source chamber turbomolecular pump.

```
1
2  # this progam sends and receives RS232 telegrams  from the MAG integra turbomolecular pump
3  # the connection to the pump is made with the RS232 service interface
4
5
6  import serial
7  import struct
8  import base
9
10
11 # create class object which is later used by the oversight server
12 class magIntegra(base.Sensor):
13
14   # during initialization the class need the serial port, which parameter to display and a
       factor with which to
15   # multiply the value returned by the pump
16   def __init__(self, port,  parameter, factor):
17     self.port = port
18     self.parameter = int(parameter)
19     self.factor = float(factor)
20
21   # this function requests the parameter from the initialization from the pump
22   def read(self):
23
24     # start a serial connection, the parameters are defined by the pump communication
       protocol
25     ser = serial.Serial(self.port,baudrate = 19200, timeout=5,  bytesize =serial.EIGHTBITS,
       parity =serial.PARITY_EVEN, stopbits =serial.STOPBITS_ONE, rtscts = False)
26
27     # set up the bytes for the telegram which is sent to the mag integra pump as a byte steam
28     STX = 2
29     LGE = 22
30     ADR = 0
31     PKE1, PKE2 = self.genPKE()
32     IND = 0 # element of parameter, not relevant
33     PZD1 = 0 # pump control, currently not used
34     STW = 0 # ! must be zero, otherwise PZD1 bits are not ignored
35
36
37     # this list represents the whole telegram, the 0 are set for reading request
38     telegram = [STX, LGE, ADR, PKE1,PKE2, 0,IND,0,0,0,0,PZD1,STW, 0,0,0,0,0,0,0,0,0]
39
40
41     # generate the last byte of the telegram, a checksum
```

```
42    # starting at the first byte the checksum is generated by iteratively XOR-ing the bytes
      together
43    checksum = STX
44    for i in range(22):
45      checksum = checksum ^ telegram[i+1]
46
47    telegram.append(checksum)
48
49    # send elements of telegram list as bytes and receive and answer (in the best case)
50    format = '<B'
51          for _ in telegram:
52                  ser.write(struct.pack(format,_))
53          rTelegram = []
54          response = ser.read(24)
55
56
57    # if there are bytes in the response build up a list of returned bytes, the rTelegram
58    for _ in response:
59                  rTelegram.append(struct.unpack(format,_)[0])
60
61    # if bytes were returned, return the parameter value
62    if(len(rTelegram)!=0):
63      PWE = rTelegram[7:11]
64            result = PWE[-4]*2**(3*8) + PWE[-3]*2**(2*8) + PWE[-2]*2**(8) + PWE[-1]
65      return str(result*self.factor)
66    else:
67      return "-1"
68
69  # this function generates the PKE bytes which are used to tell the pump which parameter to
      send
70  def genPKE(self):
71
72          parameternumber = self.parameter
73    bits = bin(parameternumber)[2:]
74          l = len(bits)
75          diff = 11-l
76          bits = '0'*diff + bits
77
78          bits = '0001' + '0' + bits
79          byte1=int('0b' + bits[:8],2)
80          byte2 =int('0b' + bits[8:],2)
81          #print("genPKE: " + str(byte1) + " " + str(byte2))
82          return byte1, byte2
```

The procedure for adding a new sensor, and general documentation of the oversight system can be found in the master thesis of Stefan Cesnik [3]. The turbomolecular pump communication protocol and the detailed meaning of the bytes in the telegrams is described in the manual

of the pump, called *Serial Interfaces for MAG integra, RS232, RS485, Profibus.*

C.3 QMS programs

In order to record the Mg pickup curves over oven current, a fully automated Matlab program (*measure_pickup_statistics_v3*) and an evaluation program (*show_QMS_pickup_stat*) was developed. The program ramps the oven current and records QMS mass currents (either for a few masses or whole mass spectrum intervals). The valve connecting the source chamber to the rest of the vacuum system is controlled by the program as well, and allows the measurement of effusive mass spectra for later subtraction from the mass spectra with the helium beam. The spectra in Figures B.1c and B.1b were recorded with this program.

For monitoring of the magnesium masses during measurements the program *mass_table_v2* was developed. The program plots the QMS currents for certain masses over time. This proved to be very useful for reproducing measurements.

C.4 Chamber Alignment LED

During chamber alignment it is helpful to shine a light through the skimmer and check if it is visible at the end of the main chamber. For this purpose a flat, Arduino powered LED was used, which can be place between the nozzle and the skimmer (see Figure C.2) A full description of the LED wiring and Arduino code can be found in the lab book entry from 17.07.20.

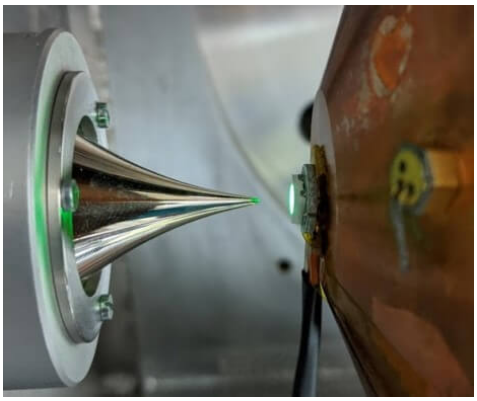

Figure C.2: The chamber alignment LED mounted between nozzle and skimmer.

Bibliography

[1] A. Apfolter. "Wiederaufbau und Test einer He–Streuapparatur und erste Streuexperimente an amorpher sowie kristalliner SiO2 Oberfläche". MA thesis. TU Graz, 2005.

[2] M. Bainschab. "Multiphoton Ionization Channels in Molecules Investigated by PEPICO Spectroscopy". MA thesis. TU Graz, 2016.

[3] S. Cesnik. "The Role of Molecular Symmetries in Non-adiabatic Relaxation Dynamics". MA thesis. TU Graz, 2018.

[4] S. Göde, R. Irsig, J. Tiggesbäumker, and K.-H. Meiwes-Broer. "Time-resolved studies on the collapse of magnesium atom foam in helium nanodroplets". In: *New Journal of Physics* 15.1 (2013), p. 015026. DOI: 10.1088/1367-2630/15/1/015026.

[5] H. Haberland, ed. *Clusters of Atoms and Molecules*. Springer Berlin Heidelberg, 1994. DOI: 10.1007/978-3-642-84329-7.

[6] P. Heim. "Analysis of molecular Rydberg state relaxation dynamics applying Bayesian probability theory". MA thesis. TU Graz, 2017.

[7] P. Heim, S. Mai, B. Thaler, S. Cesnik, D. Avagliano, D. Bella-Velidou, W. E. Ernst, L. González, and M. Koch. "Revealing Ultrafast Population Transfer between Nearly Degenerate Electronic States". In: *The Journal of Physical Chemistry Letters* 11.4 (2020), pp. 1443–1449. DOI: 10.1021/acs.jpclett.9b03462.

[8] A. Hernando, M. Barranco, R. Mayol, M. Pi, and F. Ancilotto. "Density functional theory of the structure of magnesium-doped helium nanodroplets". In: *Physical Review B* 78.18 (2008). DOI: 10.1103/physrevb.78.184515.

[9] L. Kazak, S. Göde, K.-H. Meiwes-Broer, and J. Tiggesbäumker. "Photoelectron Spectroscopy on Magnesium Ensembles in Helium Nanodroplets". In: *The Journal of Physical Chemistry A* 123.28 (2019), pp. 5951–5956. DOI: 10.1021/acs.jpca.9b02880.

[10] M. Koch, P. Heim, B. Thaler, M. Kitzler, and W. E. Ernst. "Direct observation of a photochemical activation energy: a case study of acetone photodissociation". In: *Journal of Physics B: Atomic, Molecular and Optical Physics* 50.12 (2017), p. 125102. DOI: 10.1088/1361-6455/aa6a71.

[11] P. Kruit and F. H. Read. "Magnetic field paralleliser for 2π electron-spectrometer and electron-image magnifier". In: *Journal of Physics E: Scientific Instruments* 16.4 (1983), pp. 313–324. DOI: 10.1088/0022-3735/16/4/016.

[12] F. Lackner. "Rydberg States of Alkali-Metal Atoms on Superuid Helium Nanodroplets". PhD thesis. TU Graz, 2012.

[13] H. Lauterwald and K. Rademann. "Direct Absorption Studies of Jet-Cooled Metal Dimers: Magnesium and Cesium". In: *Berichte der Bunsengesellschaft für physikalische Chemie* 96.9 (1992), pp. 1273–1275. DOI: 10.1002/bbpc.19920960940.

[14] P. Maierhofer, M. Bainschab, B. Thaler, P. Heim, W. E. Ernst, and M. Koch. "Disentangling Multichannel Photodissociation Dynamics in Acetone by Time-Resolved Photoelectron–Photoion Coincidence Spectroscopy". In: *The Journal of Physical Chemistry A* 120.32 (2016), pp. 6418–6423. DOI: 10.1021/acs.jpca.6b07238.

[15] F. Merkt and M. Quack. *Handbook of High-Resolution Spectroscopy*. WILEY, 2011. 2182 pp. ISBN: 0470066539. URL: https://www.ebook.de/de/product/8307921/frederic_merkt_martin_quack_handbook_of_high_resolution_spectroscopy.html.

[16] M. Meyer. "Nuclear Wave Packet Dynamics of Indium Dimers inside Superfluid Helium Nanodroplets". MA thesis. TU Graz, 2018.

[17] M. Meyer, B. Thaler, P. Heim, and M. Koch. "Femtosecond solvation dynamics of indium dimers inside superfluid helium nanodroplets". In: *EPJ Web of Conferences* 205 (2019). Ed. by G. Cerullo, J. Ogilvie, F. Kärtner, M. Khalil, and R. Li, p. 06005. DOI: 10.1051/epjconf/201920506005.

[18] NIST. *Magnesium Levels*. URL: https://physics.nist.gov/PhysRefData/Handbook/Tables/magnesiumtable5.htm.

[19] H. Pauly. *Atom, Molecule, and Cluster Beams I*. Springer Berlin Heidelberg, 2010. 364 pp. ISBN: 3642086233. URL: https://www.ebook.de/de/product/13924358/hans_pauly_atom_molecule_and_cluster_beams_i.html.

[20] A. Przystawik, S. Göde, T. Döppner, J. Tiggesbäumker, and K.-H. Meiwes-Broer. "Light-induced collapse of metastable magnesium complexes formed in helium nanodroplets". In: *Physical Review A* 78.2 (2008). DOI: 10.1103/physreva.78.021202.

[21] S. Ranftl. "Ultrafast Photoinduced Ejection Dynamics of Indium Atoms inside Superfluid Helium Nanodroplets". MA thesis. TU Graz, 2017.

[22] J. Reho, U. Merker, M. R. Radcliff, K. K. Lehmann, and G. Scoles. "Spectroscopy of Mg atoms solvated in helium nanodroplets". In: *The Journal of Chemical Physics* 112.19 (2000), pp. 8409–8416. DOI: 10.1063/1.481444.

[23] W. J. Stevens and M. Krauss. "The electronic structure of the ground and excited states of Mg_2^+ and Mg_2". In: *The Journal of Chemical Physics* 67.5 (1977), p. 1977. DOI: 10.1063/1.435132.

[24] B. Thaler. "Ultrafast molecular photodissociation dynamics studied with single-pulse femtosecond photoelectron-photoion-coincidence spectroscopy". MA thesis. TU Graz, 2017.

[25] B. Thaler. "Ultrafast Photoinduced Dynamics of Atoms and Dimer Molecules inside Helium Nanodroplets". PhD thesis. TU Graz, 2020.

[26] B. Thaler, P. Heim, L. Treiber, and M. Koch. "Ultrafast photoinduced dynamics of single atoms solvated inside helium nanodroplets". In: *The Journal of Chemical Physics* 152.1 (2020), p. 014307. DOI: 10.1063/1.5130145.

[27] B. Thaler, S. Ranftl, P. Heim, S. Cesnik, L. Treiber, R. Meyer, A. W. Hauser, W. E. Ernst, and M. Koch. "Femtosecond photoexcitation dynamics inside a quantum solvent". In: *Nature Communications* 9.1 (2018). DOI: 10.1038/s41467-018-06413-9.

[28] J. P. Toennies and A. F. Vilesov. "Superfluid Helium Droplets: A Uniquely Cold Nanomatrix for Molecules and Molecular Complexes". In: *Angewandte Chemie International Edition* 43.20 (2004), pp. 2622–2648. DOI: 10.1002/anie.200300611.

[29] T. Weinacht. *Time-resolved spectroscopy : an experimental perspective*. Boca Raton: CRC Press, Taylor & Francis Group, 2018. ISBN: 9781498716734.

List of Figures

List of Tables

List of Acronyms

BBO Barium Borate. 29

DFT Density Functional Theory. 11
DPS Differential Pumping Stage. 27

ES Excited State. 33

FWHM Full Width at Half Maximum. 17

GS Ground State. 33

HeDFT Helium Density Functional Theory. 15

IP Ionization Potential. 33

OPA Optical Parametric Amplifier. 28

PE Photoelectron. 11
PEPICO Photoelectron Photoion Coincidence. 70
PES Potential Energy Surface. 11

QMS Quadrupol Mass Spectrometer. 21

R2PI Resonant Two Photon Ionization. 16

SFM Sum Frequency Mixing. 29
SHG Second Harmonic Generation. 29

TDC Time Delay Compensator. 29
THG Third Harmonic Generation. 31
ToF Time of Flight. 21

Danksagung

An allerester Stelle möchte ich mich bei meinem Betreuer Ass. Prof. Dipl.-Ing. Dr.techn. Markus Koch für die Möglichkeit bedanken, in seiner Gruppe eine Masterarbeit schreiben zu dürfen. Seine unkomplizierte und persönliche Art ermöglichte eine entspannte Arbeitsumgebung sowie Diskussionen auf Augenhöhe, die erheblich beim Verstehen der physikalischen Problemstellungen halfen.

Ich möchte mich bei meinen erfahrenen Kollegen und in gewisser Weise auch Mentoren Bernhard Thaler, Leonhard Treiber und Pascal Heim bedanken, die mich in die Arbeitsweisen in den Labors eingeschult haben und auch bei anderen Fragen immer hilfsbereit zur Stelle waren.

Ich bin für die entspannte Arbeitsatmosphäre genauso dankbar wie für die anregenden Gespräche in den Kaffeepausen. Hierfür möchte ich auch meinen Kollegen Robert, Kerstin und Simon bedanken, die erst in den letzen Monaten meiner Arbeit zur Gruppe hinzugestoßen sind. Für die fast wöchentliche Versorgung mit Nudeln und Toast in der Institutsküche möchte ich mich bei Pascal und Bernhard, Roman Messner und Adrian Ruckhofer bedanken.

Ich bedanke mich auch bei der Laborausrüstung, die mir gezeigt hat wie schwierig und frustrierend Experimentalphysik sein kann, aber auch dass man aus den Schwierigkeiten am meisten lernt.

Am Ende von fünf Jahren Studium möchte ich mich bei Studienkollegen und Freunden, insbesondere Kevin Nusshold, Florian Zrim und Thomas Krenn bedanken, mit denen ich im Laufe des Studium zahlreiche Labors , Übungen und Prüfungen sowie Physikerfeste bestritten habe.

Bei meinen Eltern Peter und Elisabeth bedanke ich mich neben der finanziellen Unterstützung für den Rückhalt den sie mir immer gegeben haben. Außerdem danke ich meinen Großeltern, weil sie mir immer gezeigt haben wie Stolz sie auf mich sind, und weil ich bei ihnen immer einen ruhigen Rückzugsort habe. Bei Gudrun, Leonie, Mario und Julian bedanke ich mich, weil sie mir immer das Gefühl gegeben haben willkommen zu sein.

Ich möchte mich auch bei Mathias, Roland, Florian, Bernhard, Michael und Sven für die abwechslungsreiche und entspannende Freizeitgestaltung bedanken. Bei Martin bedanke ich mich für die musikalische Zusammenarbeit und dafür dass er seine Begeisterung für die Musik mit mir teilt.

Zuletzt danke ich dir, Jessica, für deine Unterstützung und dein Verständnis in schwierigen Zeiten sowie für den Spaß den wir zusammen haben.